The Planetary Science Journal, 6:214 (25pp), 2025 September https://doi.org/10.3847/PSJ/adf8ca

The Visibility of the Ōtautahi–Oxford Interstellar Object Population Model in LSST

Rosemary C. Dorsey[1,2], Matthew J. Hopkins[1,3], Michele T. Bannister[1], Samantha M. Lawler[4], Chris Lintott[3], Alex H. Parker[5], and John C. Forbes[1]
[1] School of Physical and Chemical Sciences—Te Kura Matū, University of Canterbury, Private Bag 4800, Christchurch 8140, New Zealand; rosemary.dorsey@outlook.com
[2] Department of Physics, P.O. Box 64, 00014 University of Helsinki, Finland
[3] Department of Physics, University of Oxford, Denys Wilkinson Building, Keble Road, Oxford, OX1 3RH, UK
[4] Campion College and the Department of Physics, University of Regina, Regina, SK S4S 0A2, Canada
[5] SETI Institute, Mountain View, CA 94043, USA
Received 2025 February 12; revised 2025 June 25; accepted 2025 July 14; published 2025 September 5

Abstract

With a new probabilistic technique for sampling interstellar object (ISO) orbits with high efficiency, we assess the observability of ISOs under a realistic cadence for the upcoming Vera C. Rubin Observatory's Legacy Survey of Space and Time (LSST). Using the Ōtautahi–Oxford population model, we show that there will be complex on-sky structure in the pattern of direction and velocity revealed by the detected ISO population, with the expected enhanced northern flux complicating efforts to derive population parameters from the LSST's predominately southern footprint. For reasonable luminosity functions with slopes of $2.5 \leqslant q_s \leqslant 4.0$, the most discoverable ISOs have $H_r \simeq 14.6-20.7$. The slope of the luminosity function of ISOs will be relatively quickly constrained by the characteristics of the LSST detected population, such as the distributions of perihelia, velocity at infinity, and discovery circumstances. Discoveries are evenly split around their perihelion passage and are biased to lower velocities. After their discovery by LSST, it will be rare for ISOs to be visible for less than a month; most will have $m_r \leqslant 23$ for months, and the window for spectroscopic characterization could be as long as 2 yr. While these probabilistic assessments are robust against model or spatial density refinements that change the absolute numbers of ISO discoveries, our simulations predict a yield of 6–51 asteroidal ISOs, which is similar to previous works and demonstrates the validity of our new methods.

Unified Astronomy Thesaurus concepts: Small Solar System bodies (1469); Interstellar objects (52); Interdisciplinary astronomy (804)

1. Introduction

Interstellar objects (ISOs) provide insight into Galactic processes, from the properties of the protoplanetary disks that generate these planetesimals to star formation histories and dynamics in the Galactic potential (A. Fitzsimmons et al. 2023). The dynamical processes operating within the Milky Way lead to a clumpy stellar velocity distribution in the solar neighborhood: a well-established set of moving groups and branches, recently made visible in exquisite resolution by Gaia (Gaia Collaboration et al. 2023). As the same dynamical processes also act on the population of ISOs as they orbit in the Galaxy, M. J. Hopkins et al. (2025) inferred that the ISO velocity distribution in the solar neighborhood has comparable substructure. However, unlike stars, ISOs are too small and faint to detect while in the reaches between stars. The substructure of the ISO population only becomes directly detectable from those objects that pass into the tiny part of the solar neighborhood that is the solar system's observable volume.

Wide-field solar system surveys are required to constrain the ISO number density and velocities in the observable volume, as highlighted by P. J. Francis (2005), N. V. Cook et al. (2016), and T. Engelhardt et al. (2017) even before the discovery of 1I/'Oumuamua. Only two ISOs are yet known: 1I/'Oumuamua (K. J. Meech et al. 2017) and 2I/Borisov (IAU Minor Planet Center 2019). Despite wide-field surveys such as Pan-STARRS, ATLAS, and Zwicky Transient Facility continuing to provide large areas of sky coverage to *r*-band depths of $m_r \sim 21.0-21.7$, obtaining a level of nondetection limits on the population, no further ISOs have been detected as of 2025 June. Deeper surveys are needed. In particular, the upcoming Vera C. Rubin Observatory's Legacy Survey of Space and Time (LSST) will provide routine coverage to $m_r \sim 24.0$ (F. B. Bianco et al. 2022): a substantial expansion of the observable volume.

Understanding the observed ISO sample requires a robust and data-driven population model. Previous models of the Galactic ISO population have assumed a Gaussian velocity distribution for ISOs in the solar neighborhood (F. L. Whipple 1975; T. A. McGlynn & R. D. Chapman 1989; A. K. Sen & N. C. Rana 1993; T. Engelhardt et al. 2017; K. J. Meech et al. 2017; D. Marčeta 2023). These assumptions have been used in previous assessments of the capabilities of the LSST for ISO detection and discovery (A. Moro-Martín et al. 2009; N. V. Cook et al. 2016; D. Marčeta 2023). However, the ISO velocity distribution the solar system can expect to encounter is highly non-Gaussian and clumpy (as inferred from Gaia by M. J. Hopkins et al. 2025), so modeling needs to consider this more realistic population.

The physical properties of the local ISO population will be an integrated contribution of their source systems (A. Moro-Martín 2018; S. Pfalzner & M. T. Bannister 2019), and could test if planetesimal processes are similar across the

Galaxy. While we infer ISO age and metallicity from the Ōtautahi–Oxford model, the distribution of ISO sizes depends on processes that are currently unconstrained. Each system produces planetesimals, which then physically evolve, for instance under a collisional cascade, to develop a size–frequency distribution (SFD) particular to that subpopulation within a system. Planetesimals may become unbound to join their system's ISO contribution in its tidal stream (J. C. Forbes et al. 2024) in any state from minimally to extensively evolved, with different ejection mechanisms significant at different stages in a planetary system's evolution; for example, stellar flybys (S. Pfalzner et al. 2021) and giant planet scattering (R. Brasser et al. 2006) occur during early stages, and a release by mass loss at the end of the star's life (W. G. Levine et al. 2023) occurs later. The population then sampled by the solar system's observable volume could therefore range from the highly unlikely case of complete contribution from a single stream, to the more-probable case that each ISO comes from the stream of a different star system (J. C. Forbes et al. 2024). Planetary formation theory can provide a set of predictions; for example, planetesimals produced by the streaming instability will follow a comparatively shallow SFD (J. B. Simon et al. 2016), but their number and mass contributed from a given stellar system depend on the stellar type and planetary architecture (A. Moro-Martín et al. 2009; and references therein). Observations, however, contribute an informative prior for steeper distributions; collisionally evolved debris disks have an SFD that is only constrained at dust sizes (B. C. Matthews et al. 2014), and the solar system small body size distributions (M. Lambrechts & A. Morbidelli 2016; A. Moro-Martín 2018; W. F. Bottke et al. 2023) overlap with the two known ISO sizes. Therefore, a range of ISO luminosity functions (and hence SFDs) must be considered.

Unlike most bound populations of solar system small bodies, ISOs transition across visibility regimes, and their survey observability is impacted by different biases. Trailing losses may significantly reduce the visibility of ISOs due to their potential high excess velocities (D. Marčeta & D. Z. Seligman 2023). This typically occurs in the near-Earth space (similar to near-Earth asteroids) where ISOs exhibit large on-sky rates of motion. At larger heliocentric distances, infalling ISOs instead have characteristics akin to trans-Neptunian discovery biases; ISO surveys must have suitable detection efficiencies throughout the heliocentric range. This behavior is somewhat shared by solar system comets, whose detection (typically at small distances; M. Królikowska & P. A. Dybczyński 2019) is aided by extended comae. However, while long-period comets are isotropic in orbital distribution to the first order, the Galactic motion of the solar system means inbound ISOs pour preferentially across the sky from the solar apex (T. A. McGlynn & R. D. Chapman 1989; D. Seligman & G. Laughlin 2018), with an on-sky distribution affected by the local three-dimensional velocity distribution.

A survey with well-understood parameters is also key to the survey simulation of ISOs. Historically, the complex observational properties of the LSST were often broadly approximated in such modeling; this was a natural outcome of the evolving creation of the cadence of the LSST, which eventually became fully community generated (F. B. Bianco et al. 2022). These parameters are now converging, in particular, precise cadence modeling now exists. M. E. Schwamb et al. (2023) provided a community assessment of its effects on a range of other solar system populations, but only qualitatively approximated ISO requirements. With first light for Rubin and the start of the LSST now approaching, it is timely to address LSST's capabilities for ISO discoveries in detail.

Here, we explore the visibility of ISOs of the Ōtautahi–Oxford ISO population model (C. Lintott et al. 2022; M. J. Hopkins et al. 2023, 2025; J. C. Forbes et al. 2024) within the specified expected cadence and seeing conditions of the LSST. We provide probabilistic predictions of the ISO observability and discovery in LSST, with transparency to our model assumptions. We also distinguish between multiple effects on observability to provide more generalized outcomes that demonstrate any survey's biases or sensitivities to ISOs. We account for a range of luminosity functions in our observability modeling. We focus on inactive ISOs rather than those with comae, as the faintest limiting case of visibility. Determining ISO physical properties will be a joint-facility effort: we predict the length of time ISOs will remain visible after their discovery by LSST, for further characterization.

2. ISO Orbital Model and Orbit Sampling

We use the Gaia-derived model of the solar-neighborhood ISO population from M. J. Hopkins et al. (2025), the current version of the Ōtautahi–Oxford model. ISO tidal streams (J. C. Forbes et al. 2024) are not anticipated to substantially shift these kinematics. In brief, a subsample of the Gaia stars (Gaia Collaboration et al. 2016, 2023) within 200 pc with measured three-dimensional velocity, metallicity, and age are debiased and reweighted to account for stellar death. This sine morte[6] population, together with a protoplanetary disk model and associated assumptions, is used to predict the joint distribution in velocity, age, and composition of ISOs in the solar neighborhood, far from the gravitational influence of the Sun. Being calculated directly from stars in Gaia DR3, it includes the complex structure of the local ISO velocity distribution, as well as the expected age and inferred water-mass fraction distribution of ISOs.

ISOs provide additional challenges for survey simulation, as their orbits are unconfined to any given volume of space. Integration of ISOs becomes more computationally expensive with increasing perihelia and the number of objects simulated. A larger heliocentric orbital volume also needs to be modeled to account for gravitational focusing, where slow-moving ISOs are brought closer to the solar system by the Sun's gravity, increasing the rate of ISOs with a low relative velocity passing through the inner solar system. Previous methods (e.g., N. V. Cook et al. 2016; T. Engelhardt et al. 2017; D. Seligman & G. Laughlin 2018; D. J. Hoover et al. 2022) account for gravitational focusing numerically, starting by sampling a large number of ISO positions and velocities from the homogeneous background distribution, unperturbed and unfocused, from a volume around the Sun that is sufficiently large to make focusing effects negligible. The resulting orbital state vectors were then integrated to produce a population of hyperbolic orbits. Within this population, the ISOs of interest are those that enter a significantly smaller "observable sphere", a heliocentric volume of space in which

[6] We continue use of this from M. J. Hopkins et al. (2023): sine morte, Latin for "without death," [ˈsiːne ˈmɔrte] International Phonetic Alphabet pronunciation, or "seen-ay mort-ay."

an object is bright enough to be observed, with a radius dependent on the expected flux depth of a sky survey and the absolute magnitude H of the objects considered. These "observable" ISOs represent a small fraction of the integrated orbits; most initialized objects never pass close enough to the Sun and Earth to be observable due to their high perihelia and faint absolute magnitudes. For example, out of the $\sim 2 \times 10^9$ objects initially synthesized by T. Engelhardt et al. (2017), only 10^6 (or $<0.1\%$) were retained after applying orbital requirements $q \leqslant 50$ au and $e > 1$. This inefficient process becomes computationally expensive when simulating a large enough population of observable ISOs to perform meaningful inference.

D. Marčeta (2023)'s "probabilistic method," which samples the perturbed positions and velocities directly within an observable sphere while analytically accounting for gravitational focusing, is significantly more efficient. However, this method only produces a sample of ISOs distributed around the Sun at a given moment (e.g., a single epoch or "snapshot"). Investigating the evolution of these objects within a time period, such as a solar system survey, requires integrating each orbit. The problem then becomes again that many sampled ISOs never enter their actual observable sphere, and the simulation must "refresh" the population as new objects move in and out of their observable sphere during the survey duration. The immediate solution would be to sample objects on an even larger sphere to encompass all objects that could potentially become observable, increasing in radius as a function of the survey duration and the maximum velocity of an ISO. D. Marčeta & D. Z. Seligman (2023) used this approach, initializing a sphere with a radius $\sim$30 au, and considering those ISOs that enter an $\sim$8 au radius[7] observable volume—but this only accounts for the motion of objects through the largest observable sphere within a single year of the upcoming LSST survey. It also limits the maximum speed of the ISOs they consider to 22 au yr^{-1} (100 km s^{-1}), although this is not physically implausible (see Figure 3 in M. J. Hopkins et al. 2025). Modeling the full 10 yr of LSST to account for ISO travel would require sampling a volume 10^3 times greater; thus, scaling this method to future longer surveys would result in the same problem of inefficiency as earlier.

We take inspiration from the probabilistic method of D. Marčeta (2023) to construct a new ISO orbit initialization method. Rather than initializing ISOs by sampling positions and velocities so that they can be propagated along their orbits, we sample their orbits directly using the Ōtautahi–Oxford model velocity distribution. The result is that every sampled ISO orbit enters its observable sphere at some time during a survey, accounting for the probabilistic distributions of orbital parameters, realistic non-Gaussian velocity distribution, and gravitational focusing. This allows us to include nonzero lengths of time, and therefore avoid the need to sample ISOs in a larger volume of phase space than is realistically observable. We simulate the full 10 yr LSST survey with no upper limit on ISO speed and a much larger volume observable sphere, which we set to the radius 100 au. As in D. Marčeta (2023), the orbits drawn are parameterized by their preencounter velocity, denoted with a heading in Galactic longitude and latitude l, b and a speed at infinity v_∞, as well as an impact parameter B, and position angle φ. The distribution of orbits in these

[7] This corresponds to a maximum object diameter of 1 km.

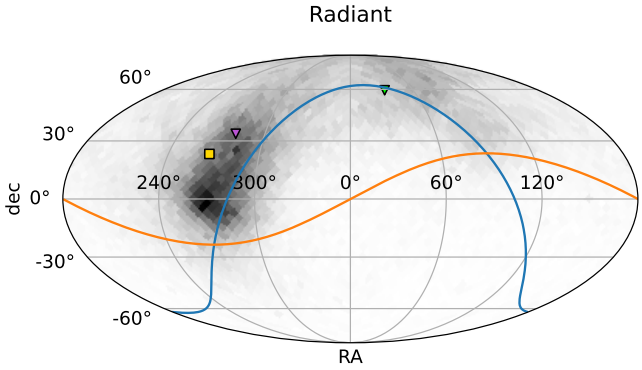

Figure 1. Ōtautahi–Oxford model distribution of ISO radiants, the directions ISOs approach the solar system from on the celestial sphere. The blue and orange lines indicate the Galactic and ecliptic planes, respectively. The solar apex (yellow square), and the incoming radiants of 1I/'Oumuamua (pink triangle) and 2I/Borisov (green triangle) are also indicated.

parameters depends only on the survey length T and the radius of the observable sphere r, set by the minimum H of the objects to be considered, and we derive this distribution here. The flux of ISOs onto an orbit (l, b, v_∞, B, φ) is given by D. Marčeta (2023) Equation (11):

$$F_{l,b,v_\infty,B,\varphi} = \frac{dN}{dl\ \ db\ \ dv_\infty dB\ \ d\varphi\ \ dt} = nBv_\infty p_{l,b,v_\infty} \quad (1)$$

where n is the ISO spatial number density, and p_{l,b,v_∞} is the velocity distribution of ISOs in the solar neighborhood, far from the gravitational influence of the Sun, for which we use the Ōtautahi–Oxford model for the underlying velocity distribution. This is derived in detail in Section 2.3 of M. J. Hopkins et al. (2025) and plotted in their Figure 6 in Galactic coordinates; for ease of reading in this work, we plot the distribution of radiants of that velocity distribution in equatorial coordinates in Figure 1.

The number of objects on a given orbit that will spend any length of time within the observable sphere during the survey of the length T is equal to the sum of those in the sphere when the survey begins, plus the number that flow in over the time T. On the timescale of a survey, the flux of ISOs is constant (S. Portegies Zwart 2021; J. C. Forbes et al. 2024), meaning this fluence is equal to

$$\frac{dN}{dl\ \ db\ \ dv_\infty dB\ \ d\varphi} = (t_{\rm res}(v_\infty, B, r) + T) F_{l,b,v_\infty,B,\varphi} \quad (2)$$

for the residence time $t_{\rm res}(v_\infty, B, r)$, defined as the time spent by an object on a given orbit inside the observable sphere of the radius r. An analytic expression for this and the integrals required for sampling this distribution are given in Appendix A. For $T = 0$, this reduces to the distribution of orbits of ISOs within a sphere of the radius r at a single moment in time, i.e., the distribution of D. Marčeta (2023). For $T \gg t_{\rm res}$, the ISOs already in the sphere when the survey begins are negligible compared to those that flow in over the survey, so the distribution is dominated by the refreshing population—this is the volume-sampling weighted distribution used in J. C. Forbes & A. Loeb (2019) and M. J. Hopkins et al. (2025; e.g., $q < 5$ au in their Table 1 would correspond to this distribution's $r = 5$ au).

Drawing l, b, v_∞, B, and φ from the distribution in Equation (2) produces a sample of orbits; we detail the method in Appendix A. To sample the positions of ISOs along these orbits, we choose the time of the perihelion passage τ relative to the start of the survey at the time $t = 0$. For each orbit, we sample this from Uniform$(-t_{\rm res}/2,\ \ t_{\rm res}/2 + T)$. For example, an ISO with $\tau = -t_{\rm res}/2$ had its closest approach to the Sun at the time $t = -t_{\rm res}/2$, and is outgoing on the edge of the observable sphere by the start of the survey at $t = 0$. Similarly, an ISO with $\tau = T + t_{\rm res}/2$ has its closest approach to the Sun at $t = T + t_{\rm res}/2$, and only just enters the observable sphere at the end of the survey $t = T$.

For computational simplicity, our method ignores some effects that will change the distribution of ISO orbits in a small way. First, unlike D. Marčeta (2023), we ignore the negligible possibility that an ISO may not complete its solar system passage due to an impact or close encounter with the Sun (similar to a Sun-grazing comet). For example, for $H_r = 23$ objects within a ∼2.16 au observable sphere, only 1 in $\sim 10^8$ objects of an isotropic ISO population would have orbits crossing the solar Roche limit for asteroids ($1.28R_{\rm Sun}$ for an asteroidal density; B. Gundlach et al. 2012). This fraction decreases further for smaller values of H_r as the observable sphere increases in radius. In Section 4, we confirm $\leqslant$0.02% of discovered ISOs will be sungrazers. Second, we assume all ISOs follow perfectly hyperbolic orbits about the solar system barycenter, and thus ignore nongravitational accelerations (i.e., cometary activity), deviations from Newtonian gravity due to general relativity, or close encounters with planets.

2.1. Preparing the ISO Model for Observability Simulations

Sampling ISO orbits within only one observable sphere over a multi-year-long survey is inefficient for understanding population characteristics, as the resulting population will be dominated by small objects on orbits too distant to be observable. The maximum observable heliocentric distance in an astronomical unit, $r_{\rm h}$, of an object at opposition is related to its absolute magnitude H_r and apparent r-band magnitude m_r by

$$r_{\rm h} = \frac{1}{2}(1 + \sqrt{1 + 4 \times 10^{(m_r - H_r)/5}}) \quad \text{(au)}. \tag{3}$$

For example, the maximum observable sphere to $m_r = 25$ would be $r_{\rm h} \sim 100$ au for $H_r = 5$, or $r_{\rm h} \approx 1.6$ au for $H_r = 25$. However, for an isotropic distribution of ISO orbits within a ∼100 au sphere, only 1 in ∼244,000 objects with $H_r = 25$ (or 0.0004%) would ever be observable during any part of their orbit. This presents a large computational inefficiency.

To improve this, we divide the H_r range that we will consider ($5 \leqslant H_r \leqslant 23$, Section 3) into 1 mag intervals, and for each interval sample orbits passing through the observable sphere with the radius $r_{\rm h}$ corresponding to the largest objects (minimum H_r) of each bin. This increases the proportion of observable objects in each H_r interval with which to perform inference. We draw 10,000 orbits in each 1 mag H_r interval for $5 \leqslant H_r \leqslant 13$ and 50,000 orbits in each 1 mag H_r interval for $13 \leqslant H_r \leqslant 23$.

To compare these samples from different H_r intervals as if they were drawn from the one observable sphere and one H_r interval, they must be reweighted. For each H_r interval, this weighting is proportional to the number of objects within the H_r interval expected to enter the corresponding observable sphere. The total number of objects entering an observational sphere of radius is given by the integral over $\boldsymbol{v}_\infty$ of Equation (A5), which being nonanalytic we approximate well with $n \cdot \left(\frac{4}{3}\pi r_{\rm h}^3 + \pi r_{\rm h}^2 T(0.029 \text{ au day}^{-1})\right)$ (see Figure 18 in Appendix A). The fraction of these objects within the corresponding size interval $H_r = [H_{\rm min}, H_{\rm max}]$ is proportional to $(10^{\alpha H_{\rm max}} - 10^{\alpha H_{\rm min}})$, for a given single-slope absolute magnitude distribution $dN/dH \propto 10^{\alpha H}$. Thus, the total weight w given to each H_r interval is given by

$$w \propto (10^{\alpha H_{\rm max}} - 10^{\alpha H_{\rm min}})\left(\frac{4}{3}\pi {r_{\rm h}}^3 + \pi {r_{\rm h}}^2 T(0.029 \text{ au day}^{-1})\right). \tag{4}$$

3. Simulating ISO Observability within the LSST

While we aim to identify common concerns for ISO visibility in sky surveys with our model, the primary survey we consider here is Rubin's LSST. This 10 yr survey with the 8.4 m Simonyi Survey Telescope is expected to reach a single-image depth of $m_r \sim 24.0$ across some 18,000 deg^2 of predominantly southern sky (LSST Science Collaboration et al. 2009; F. B. Bianco et al. 2022). For our assessment of the visibility of ISOs, we use the LSST cadence simulation `baseline_v3.3_10yrs` (E. Naghib et al. 2019; P. Yoachim & M. R. Becker 2023), the most realistic available during this work; the small changes since[8] affect neither the footprint nor filters of primary ISO detectability. Future cadence simulations may employ a single 30 s exposure rather than two 15 s exposures per visit; this will result in slightly deeper single-exposure limiting magnitudes and free up an additional ∼8% of survey time for additional visits, which may increase the visibility of ISOs.

Our approach is to consider and identify the major influences on the probabilistic observability of our probabilistic ISO velocity model. We construct a set of nomenclature:

1. visited, a probabilistic ISO orbit is within an LSST field of view (FOV);
2. observed, a probabilistic ISO orbit with physical properties applied would be an $\geqslant 5\sigma$ source in an LSST image, forming an observation;
3. discovered,[9] a minimum set of LSST observations exist for an observed ISO that meets particular discovery requirements;
4. arc length, the period between the first and last observations of an ISO by LSST;
5. characterization window, the period that an ISO has brightness $m_r \leqslant m_{\rm interest}$ after it is discovered for some defined magnitude cutoff $m_{\rm interest}$.

We first assess whether our ISOs are present within the FOV of LSST at the time of each observation in `baseline_v3.3_10yrs`. For this, we evaluate the position of the ISO along its orbit at the time of the pointing (using the method of D. Farnocchia et al. 2013), and check if the ISO lies within a cone of the opening angle $\theta_{\rm FOV} = 1.^\circ75$ pointing from the Earth's position at that time. This assumes a simplistic circular FOV with the same 9.6 deg^2 area as the LSST FOV but

[8] As of the Phase 3 Recommendation (LSST Survey Cadence Optimization Committee 2024).

[9] The formal LSST nomenclature uses "detect" for this term, but since we are discussing multiple aspects of detectability, we use "discovered" for clarity.

Table 1
Values for the Trailing Loss Coefficients in Equation (5)

Trailing Loss Type	Coefficient	
	a	b
SNR only	0.67	1.16
SNR and Detection	0.42	0.00

ignoring the complex shape of the detector and chip gaps. We additionally assume that objects remain within the FOV for the whole exposure. We make use of the hyperbolic nature of ISO orbits to increase the computational efficiency of this step by skipping pointings guaranteed not to be visited: for orbits with perihelion $q > 1$ au, these are pointings perpendicular to the plane of the orbit and pointings directly away from perihelion, extending to any pointings within an angle of $\arccos(1 \text{ au}/q) - \theta_{\rm FOV}$ of the perpendicular to the orbit, and any pointings within an angle of $\arccos(1/e) - \theta_{\rm FOV}$ of the direction away from perihelion. Our method does not require any numerical integration to capture the effect of (1) short-term (e.g., cometary activity) or (2) long-term perturbations (e.g., gravitational perturbations) to an ISO's orbit because (1) we are interested in the characteristics of the ISO population and not the detailed understanding of an individual ISO, and (2) each ISO only performs one orbit through the solar system, so the cumulative effects of long-term perturbations can be considered negligible. If a given ISO meets these criteria for at least one pointing, it is visited.

Once an ISO's orbital geometry has meant it is visited, we apply physical properties to determine whether it is observed. An object's apparent magnitude in an LSST filter band at any given time is described by

$$m_{\rm filter} = H_r + \underbrace{5\log_{10}(r_{\rm h}\Delta)}_{\Delta m_{\rm dist}} + \underbrace{|2.5\log_{10}(\Phi)|}_{\Delta m_{\rm phase}} + \underbrace{\left|1.25\log_{10}\left(1+\frac{ax^2}{1+bx}\right)\right|}_{\Delta m_{\rm trail}} + \underbrace{(m_{\rm filter}-m_r)}_{color} \quad (5)$$

$$x = \frac{\mu T_{\rm exp}}{24\theta} \quad (6)$$

where H_r is the absolute magnitude (we use r band for consistency), $r_{\rm h}$ is the heliocentric distance in astronomical units, Δ is the geocentric distance in astronomical units, Φ is the phase function evaluated at phase angle α, and a and b are trailing loss coefficients with values given in Table 1. The variable x is a function of the on-sky rate of motion μ in degrees per day, the image exposure time $T_{\rm exp}$ in seconds, and the median seeing θ in arcseconds. The variables $T_{\rm exp}$ and θ are provided by the LSST cadence simulation for each observation. We factorize Equation (5) into five independent terms, describing the effect of morphologic (H_r), geometric ($\Delta m_{\rm dist}$, $\Delta m_{\rm phase}$), kinematic ($\Delta m_{\rm trail}$), and compositional (color) characteristics of ISOs on their observed apparent magnitude. The inverse-square distance effects on brightness ($\Delta m_{\rm dist}$) are straightforward, but the other terms have additional complexities.

The absolute magnitude of an individual object is a direct result of its physical characteristics, including size (diameter D in kilometers), dimensions (axis ratio a:b:c), and surface reflectivity (albedo p, which is dependent on composition). These properties are influenced by disk formation location, planetesimal growth efficiency, collisional evolution, and thermal processing. Their impact on the characteristics of individual ISOs and their overall Galactic population is currently unconstrained. While well explored for solar system small body populations, with only two known ISOs (e.g., D. Jewitt & D. Z. Seligman 2023), the parameter space is open. For simplicity, we consider a single-slope power law and test a range of slope values $q_s = [2.5, 3.0, 3.5, 4.0]$ that bracket the streaming instability-like SFD ($q_s = 2.8$, J. B. Simon et al. 2016). These cover a range of values from the absolute magnitude distributions of different solar system small body populations, including asteroids (W. F. Bottke et al. 2005; A. Alvarez-Candal & J. Licandro 2006), Kuiper Belt objects (J.-M. Petit et al. 2023), as well as the predicted primordial planetesimal disk (W. F. Bottke et al. 2023). The minimum value for q_s is set to the critical value below which larger objects are more-probable discoveries than smaller objects; see Appendix B for a detailed derivation. We include the streaming instability size distribution $q_s = 2.8$ in our analysis for several reasons. First, the majority of circumstellar material is ejected from its planetary system during the early stages of planet formation and evolution (J. A. Fernandez 1978; H. F. Levison & M. J. Duncan 1997; S. N. Raymond et al. 2020; A. Fitzsimmons et al. 2023) and therefore has potentially undergone minimal processing via collisional or thermal effects. Additionally, our ISO model (Section 2) assumes that the age of an ISO is directly correlated to the age of the star that produced it.

We assess observability for objects with absolute magnitudes $5 \leqslant H_r \leqslant 25$, corresponding to ISOs of a size $0.07 \lesssim D \lesssim 600$ km for an assumed asteroidal albedo $p_r = 0.05$ (J. Licandro et al. 2016; J. R. Masiero et al. 2021). For context, the upper limit corresponds to the minimum diameter at which internal differentiation could be expected, also used for an object to be classified as a rocky dwarf planet (C. H. Lineweaver & M. Norman 2010), while the lower limit encompasses the sizes of the two known ISOs, a radius of ~100 m for 1I/'Oumuamua ('Oumuamua ISSI Team et al. 2019) and ~0.5 km for 2I/Borisov (M.-T. Hui et al. 2020; D. Jewitt et al. 2020), as well as the expected LSST r-band single-image 5σ limiting magnitude ($m_5 \sim 24.0$; F. B. Bianco et al. 2022).

Other parameters that influence the absolute magnitude distribution of ISOs include the size D, albedo p_r shape a:b:c, aspect angle, and light-curve amplitude. While the size and shape of 1I/'Oumuamua are reasonably well constrained by its light curve ('Oumuamua ISSI Team et al. 2019), their values for the nucleus of the cometary ISO 2I/Borisov are only inferrable from the physical extent of its coma and the nongravitational perturbations to its orbit, with both methods requiring assumptions for the nucleus composition, albedo, density, and structure. The albedos of the known ISOs are estimated to be in the range $p \sim 10^{-2}$–10^{-1} (M. T. Bannister et al. 2017; D. E. Trilling et al. 2017; D. Jewitt & J. Luu 2019); however, the true values are not well constrained. Additionally, there exists a correlation between size and shape among solar system objects with $D > 1$ km (e.g., main-belt asteroids,

M. Mommert et al. 2018); however, for small objects $D < 200$ m, this relationship remains uncharacterized (A. Thirouin et al. 2018; A. McNeill et al. 2019; A. K. Mainzer et al. 2023). Thus, while the extreme light-curve variability of 1I/'Oumuamua undoubtedly influenced its observability (W. G. Levine & R. Jedicke 2023; see also Section 7.1), it is unwise to extrapolate the ISO shape distribution from a single known value. This is particularly important since 1I/'Oumuamua was found to be in a tumbling state (W. C. Fraser et al. 2018), and the rotation of 2I/Borisov is unconstrained; thus, the impact of aspect angle (S. L. Jackson et al. 2022) on ISO observability is currently unknown for the Galactic population. Therefore, we leave the parameters of albedo, shape, aspect angle, and light-curve amplitude independent in our modeling, which only impact ISO observability via their relation to absolute magnitude.

For the geometric effect $\Delta m_{\rm phase}$, we calculate the phase function $\Phi = \Phi(\alpha)$ assuming a spherical solid body of uniform albedo using the Henyey-Greenstein model with $G = 0.15$ (Equation (36) in E. Bowell et al. 1989). The phase functions of minor planets are well explored (M. Colazo et al. 2021; M. M. Dobson et al. 2023; A. Alvarez-Candal 2024; J. E. Robinson et al. 2024a); however, defining relationships that accurately model the opposition surge (or lack thereof, e.g., V. G. Shevchenko et al. 2012) for all populations remains a work in progress. The minimal phase angle coverage of both known ISOs during their solar system passages resulted in little information on their phase functions (W. C. Fraser et al. 2018; X.-P. Lu & D. Jewitt 2019; C. Opitom et al. 2019; J. de León et al. 2020). In particular, the orientation and timing of their trajectories relative to the Earth meant that neither was observed near $\alpha = 0°$, where the opposition surge significantly impacts the phase function. In addition to the sparsely sampled phase angles, the phase function is also dependent on color, albedo, shape or axis ratio (acute for 1I/'Oumuamua see S. Mashchenko 2019, but less pronounced for other small body populations, and not known for 2I/Borisov), and cometary activity (seen strongly for 2I/Borisov; e.g., M. T. Bannister et al. 2020; but only at upper limits for 1I/'Oumuamua; M. Micheli et al. 2018). Since ISOs are expected to be observed across a wide range of phase angles in LSST, we assume a simplistic phase function model until their phase behavior is better characterized.

We next consider the kinematic losses. These are directly tied to the velocity distribution of our input ISO model. Trailing loss $\Delta m_{\rm trail}$ is the reduction in the observed apparent magnitude of an object due to its on-sky rate of motion relative to the telescope tracking (R. L. Jones et al. 2018). This appears in photometric images as a nonstellar point-spread function (PSF) distribution of flux, or "trail." Trailing loss has two effects on the detectability of an object in a given exposure. The first is an inherent reduction in the signal-to-noise ratio (SNR), due to the signal spreading over a larger area of background noise pixels than a stationary source. The second effect, detection loss, is due to the nonoptimal use of a circular PSF to identify new sources, which does not fully encapsulate the total flux of the target. Unlike SNR trailing loss, it is possible to prevent detection loss by adapting the shape of the PSF used in the source detection software to account for a large on-sky motion. The primary Rubin LSST source detection pipeline does not use nonstellar PSF filters (M. E. Schwamb et al. 2023).[10] Detection losses must therefore be considered when modeling the detectability of ISOs as sources in LSST visits. Trailing loss is typically negligible for objects in the outer solar system, which have very slow on-sky velocities on the order of $\sim 1''\,{\rm hr}^{-1}$, but needs to be considered from the orbit of Mars inward. The observability of objects with large on-sky velocities on the order of $\sim 0.^{\circ}1-10^{\circ}\,{\rm day}^{-1}$ (such as ISOs at $r_{\rm h} < 1$–2 au) will thus be impacted by trailing losses.

While solar system small bodies display a wide range of colors in the optical-near-IR, there is only one surface color measurement for the known ISO population. 1I/'Oumuamua was observed to be red, similar to Jupiter Trojans, Jupiter family comets, and long-period comets (M. T. Bannister et al. 2017; D. Jewitt et al. 2017), while the nucleus of 2I/Borisov was obscured by its coma for its entire observable passage through the solar system; hence, the color distribution of the intrinsic ISO population is unconstrained. We tested the sensitivity of ISO discovery in LSST to the LSSTCam *ugrizy* distributions for solar, S-type, C-type, D-type, and CCKBO asteroidal surface types (C. N. A. Willmer 2018; M. E. Schwamb et al. 2023). We found no significant correlations between color and the likelihood of discovery, and the orbital and physical properties of the discovered ISOs. Hence, we adopt a solar spectral type for ISOs in this work.

We do not directly model satellite streaks and their complex impact on source detection in LSST images (J. A. Tyson et al. 2020; J. A. Hu et al. 2022). Instead, we performed a preliminary analysis of the influence of randomly dropped observations on ISO discovery in LSST, to approximate the discovery losses due to various phenomena that we do not model in this work (e.g., difference imaging artifacts, saturated stars, CCD chip gaps, etc.). Observations were removed with 5% probability near the Galactic plane and 1% probability elsewhere. Although discovery rates decreased by ∼2%−5% (increasing with slope q_s), no significant biases in the resulting orbital or physical parameters of the discovered ISO population were identified.

The probability of an object being observed in a given image is then given by

$$P = \left[1 + \exp\left(\frac{m - m_5}{\sigma}\right)\right]^{-1} \tag{7}$$

where m is the object's apparent magnitude in the given filter band (any of *ugrizy* for LSST), m_5 is the 5σ limiting magnitude in the given filter band, and σ is the width of the completeness falloff. The LSST pipeline computes sources by subtraction of individual survey images against a template of each region of the sky that will be developed from the first year of survey operations. During template generation in Year 1, "real-time" discoveries will be reduced (J. E. Robinson et al. 2024b); these discoveries will be recovered from data reprocessing at the end of the year for DR1. We assume detection occurs within a single image with differencing from the template as per the LSST Solar System Processing (SSP), i.e., there is no application of shift-and-stack for object detection to deepen the 5σ limiting magnitude. We assume $\sigma = 0.12$, in accordance with R. L. Jones et al. (2018). An object's detection probability P is calculated for each visit in an LSST image. These probabilities are randomly sampled to produce a set of visits where the object is observed.

[10] The subsequent LSST Solar System Processing uses trailed PSFs to link observations, however.

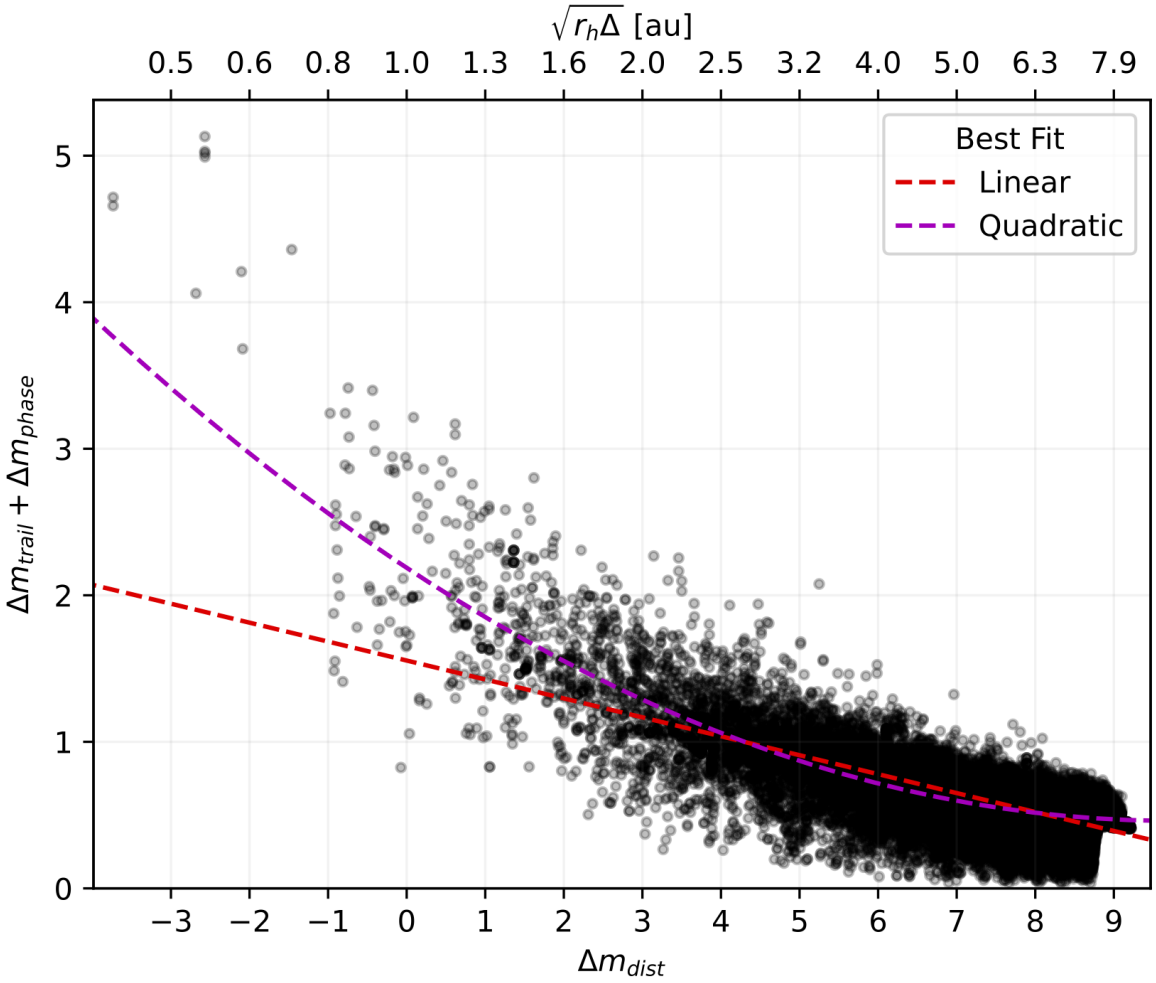

Figure 2. Combined effect of phase function and trailing loss as a function of $\Delta m_{\rm dist}$. The top x-axis indicates the geometric mean distance to the object, which affects the second term of Equation (5). Best fits using a first-order and second-order polynomial are provided for qualitative reference only. The trend is almost linear but diverges near the inner solar system ($\Delta m_{\rm dist} \lesssim 4.0$). Note that this relationship is independent of morphological effects such as absolute magnitude (H_r) and color.

3.1. Effects on Observability

To better qualitatively understand the effect of different brightness variation mechanisms on the observational probability of ISOs, we first consider a preliminary population of 10,000 ISO orbits initialized within a single heliocentric sphere of the radius 8 au. We assign a constant absolute magnitude $H_r = 17.4$ to each orbit; for an assumed albedo, e.g., $p_r = 0.05$, this corresponds to a diameter of $D \sim 2$ km. We only consider images acquired in the first year of LSST.

We first consider the relationship between distance and the secondary apparent magnitude loss due to phase and trailing. Unlike most other small body populations, a hyperbolic ISO orbit can have any orientation, so observations can be made at any phase angle $\alpha \in [0, \pi]$ with potentially large on-sky velocities $\mathcal{O}(^\circ/d)$. This means that a simple distance-based limiting magnitude systematically overestimates the maximum observable distance of an ISO. Figure 2 demonstrates how the combined effect of trailing loss and phase varies with distance, independently of an object's absolute magnitude. The relationship appears linear for large $\Delta m_{\rm dist}$ and $\sqrt{r_{\rm h}\Delta}$, but diverges for $\Delta m_{\rm dist} \leqslant 4$. This means that objects at small heliocentric and geocentric distances will be disproportionally more affected by phase and trailing losses than objects at large distances. At $\Delta m_{\rm dist} = 2.0$, the combined phase and trailing losses deviate by $\sim$0.25 from the linear approximation. This corresponds to objects with a maximum observable heliocentric distance of $r_{\rm h} \approx 2.16$ au, or $H_r \approx 23$. We take this as an effective "limiting absolute magnitude" for ISOs within LSST, and all further analysis in this work uses $H_r \leqslant 23$.

We then consider the effect of the geometric viewing and kinematic losses on the probability that an ISO is observed in an LSST image. Unsurprisingly, the dominant effect on ISO observability is from their distance at observation (Figure 3). However, phase and trailing losses also affect observability. For the same $\Delta m_{\rm dist}$, images taken at high phase angles with high on-sky motions are less likely to produce a successful ISO observation than images taken at low phase angles with low on-sky motions. An additional interesting feature of Figure 3 is the lack of a strict boundary between regions of the parameter space where ISO are observable and unobservable. This is due to the variation in the 5σ limiting magnitude and seeing between individual LSST observations. These variations model the real-world physical phenomena that will affect the LSST cadence (e.g., seasonal weather patterns, airmass variations, etc.), hence creating a complex relationship between the three variables in Figure 3.

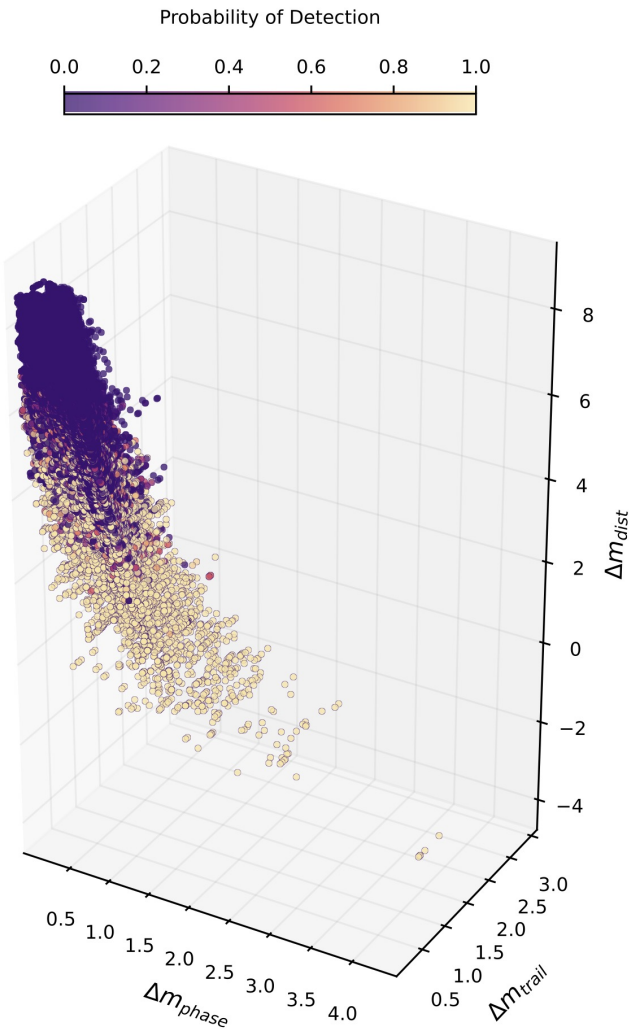

Figure 3. Influence of the geometric and kinematic observational biases on the detection probability of all instances where an ISO's orbital position is synchronized with the LSST cadence. The axes refer to the last three terms in Equation (5), corresponding to the change in apparent magnitude of an object due to distance ($\Delta m_{\rm dist}$), geometric viewing ($\Delta m_{\rm phase}$), and trailing loss ($\Delta m_{\rm trail}$). The nonlinearity in the transition from completely observable ($P = 1$) to completely unobservable ($P = 0$) ISOs is due to the seeing and limiting magnitude varying across all LSST images.

3.2. Discoverability

We assess the discoverability of ISOs within the context of LSST SSP (J. Myers et al. 2013; M. Juric et al. 2020; C. F. Claver & LSST Systems Engineering Integrated Project Team 2024). The criteria for the discovery of a moving object are defined by the Observatory System Specifications requirement OSS-REQ-0159 (C. F. Claver & LSST Systems Engineering Integrated Project Team 2024), which we list verbatim, an object is discovered by the LSST SSP $\geqslant 95\%$ of time when it is observed in the following pattern:

1. over 15 days, the object is observed on at least three separate nights, with at least one tracklet per night, where
2. a tracklet is defined as two or more observations taken in an interval not longer than 90 minutes where an object's astrometric position has changed by $\geqslant 3\sigma$ (where $\sigma \approx 140$ mas is the positional astrometry uncertainty; R. L. Jones et al. 2018; M. E. Schwamb et al. 2023), and
3. each observation being defined as a source registering above the 5σ threshold after convolution with the image's PSF (as required by LSST source detection).

Data security standards designed to restrict the collection of information on artificial satellites may provide additional constraints on ISO discovery in LSST; moving objects with streaks $\geqslant 10^\circ\,{\rm day}^{-1}$ will not be alerted in the regular channels (W. O'Mullane et al. 2024).

The above criteria apply to the main survey, comprised of the "Wide-Fast-Deep" and the Deep Drilling Fields, but break down for the fraction of LSST observations performed during the low-elongation twilight survey every few nights. This microsurvey targets small solar system bodies that spend limited time within the main LSST footprint, including objects with fast on-sky motion rates (such as Near-Earth Objects, "NEOs", or ISOs) as well as inner Earth orbital populations (e.g., the recently discovered 'Ayló'chaxnim asteroid population; B. T. Bolin et al. 2020, 2022), which are only observable within the twilight survey. The analysis by M. E. Schwamb et al. (2023) showed that less stringent and more conventional object detection methods such as three or four observations within the same night could significantly improve the discovery completeness for such fast-moving objects. Thus, in addition to the standard LSST SSP detection criteria employed for the main survey, we assume that observing an object in four twilight visits within the same 90 minute interval is sufficient for its discovery (K. Volk 2025, personal communication, SCOC).

ISOs are expected to exhibit a large range of on-sky rates of motion as they pass through the solar system, due to their high hyperbolic excess velocities (see Figure 3 in M. J. Hopkins et al. 2025). Although LSST will be capable of linking large trails ($\gtrsim 1^\circ\,{\rm day}^{-1}$; R. L. Jones et al. 2018), the on-sky motion rate is typically conservatively constrained to $\sim 0.^\circ 5\,{\rm day}^{-1}$ for computational efficiency. Additionally, discovery requires a minimum on-sky motion of $\gtrsim 0.''3\,{\rm hr}^{-1}$ for a moving object (Section 3.2). This potentially raises concerns about the linking of ISO tracklets. Figure 4 explores the range of on-sky motion rates for each LSST visit to simulated ISOs with perihelia $q \leqslant 5$ au. In more than 95% of visits, the ISO has on-sky velocity $\leqslant 150''{\rm hr}^{-1}$ (or $1^\circ\,{\rm day}^{-1}$), while >90% of all visits to all simulated ISOs have on-sky velocities $\leqslant 100''{\rm hr}^{-1}$. Additionally, in at least 99% of visits, ISOs with $q \leqslant 5$ au will have on-sky motion rates and accelerations consistent with bound solar system objects (including outer solar system planets and NEOs) and the two previously observed ISOs, as well as being above the minimum threshold for LSST SSP. Thus, we can expect only a tiny fraction of LSST visits will be to ISOs exhibiting high on-sky motion rates, and these are restricted to orbits with perihelia $q \leqslant 5$ au; in Section 4, we confirm with our simulations $\leqslant 0.05\%$ of discoveries will have an on-sky motion faster than the LSST SSP threshold of $10^\circ\,{\rm day}^{-1}$. We therefore assume SSP's linking is consistently successful.

4. Constraints on the ISO Size–Frequency Distribution

The discovery efficiency of LSST is significantly incomplete for ISOs, even within the inner solar system. Of the ISOs observed by LSST (i.e., objects with at least one visit), 35.2%–62.2% have $\geqslant 6$ detections, and 27.9%–52.8% have $\geqslant 3$ tracklets in the main survey, with the steepest absolute

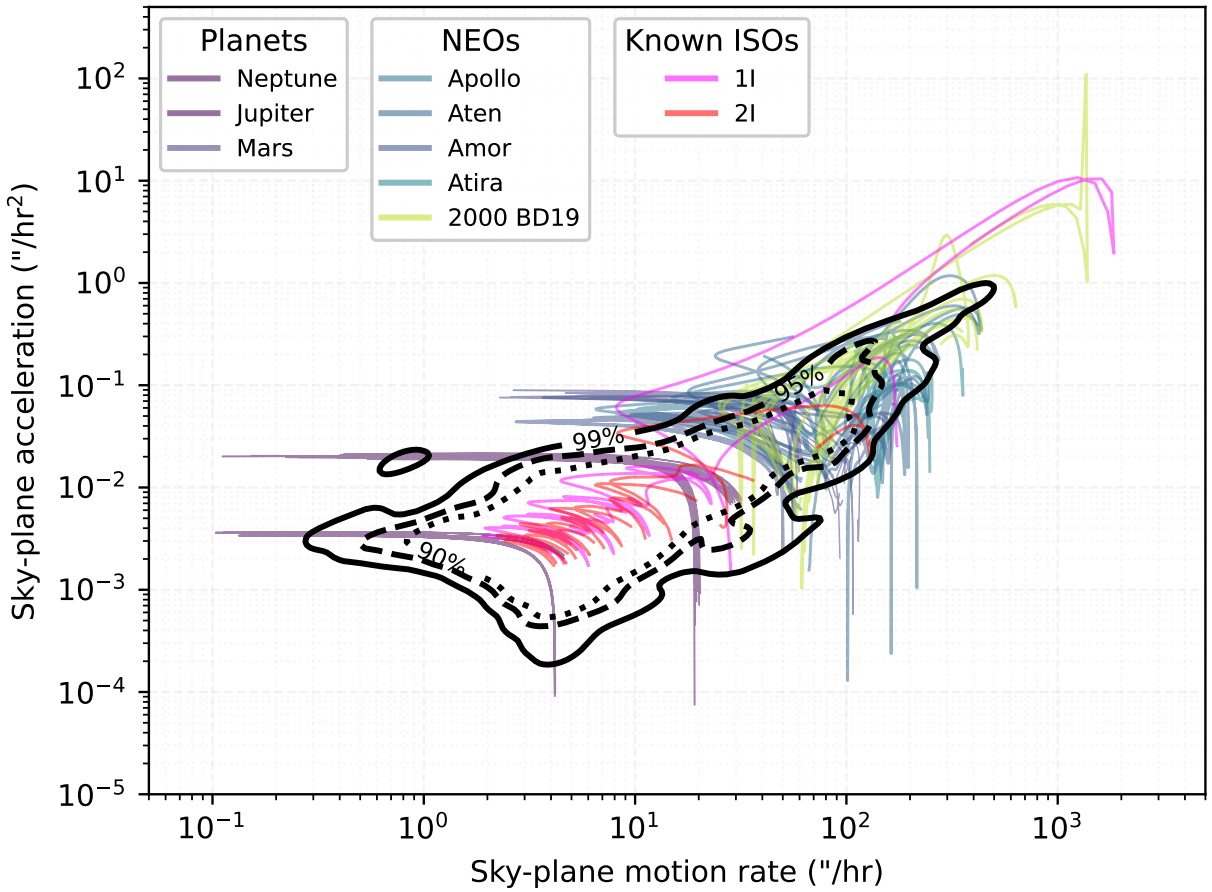

Figure 4. Expected on-sky rates of motion and acceleration for simulated ISOs with $q \leqslant 5$ au (black contours) within LSST visits, regardless of whether they are observed in an image, compared to a selection of bound solar system objects and the two known ISOs. The regions of the on-sky velocity–acceleration phase space containing 90%, 95%, and 99% of all simulated ISO visits are traced by dotted, dashed, and solid lines, respectively. The planets and NEOs were simulated over the 10 yr duration of LSST using ephemerides from JPL Horizons, whereas 1I/'Oumuamua and 2I/Borisov were simulated for the same duration but centered around their perihelion passage through the solar system. Objects with low perihelia appear toward the top right, while objects with high perihelia appear toward the bottom left; Neptune has the slowest on-sky motion rate of all the bound solar system objects. Note that an on-sky rate of motion of 1° day^{-1} is equivalent to 150″hr^{-1}. While the on-sky motion of the ISO population spans multiple orders of magnitude in both velocity and acceleration phase space, the expected range for ⩾99% of ISO visits is completely compatible with the collection of bound objects in the solar system.

magnitude slope $q_s = 4.0$ population being the least visible. The fraction of observed objects that result in LSST discoveries is shown in Figure 5. Even for the largest ISOs, observed objects are only discovered ∼50% of the time. The discovery completeness decreases for smaller objects with $H_r \geqslant 13$, reaching <10% for the smallest of these ($H_r \geqslant 22$). Across all H_r values, <40% of the ISOs observed in at least one LSST image will be discovered, with the largest slope parameter $q_s = 4.0$ model being the least discoverable population at <20%.

Summary statistics for the absolute magnitude probability density functions of observed and discovered ISOs in LSST are shown in Figure 6. As the slope q_s increases, the distributions become narrower, and the median shifts to higher values of H_r, for both observed and discovered objects. The most probable discoveries have $H_r = 14.6-20.7$ for the slopes $2.5 \leqslant q_s \leqslant 4.0$. This result implies that the most frequently discovered absolute magnitude will be a tracer of the intrinsic distribution's slope parameter q_s. Perhaps surprisingly, if 1I/'Oumuamua was discovered in LSST, its absolute magnitude ($H_r \sim 22.4$; 'Oumuamua ISSI Team et al. 2019) would be consistent with all of our model H_r distributions within 2σ. On the contrary, discovering a single large ISO with $H_r \leqslant 10$ would strongly implicate a shallower slope ($q_s \leqslant 3.0$) for the intrinsic absolute magnitude distribution.

From our simulated discovery rates, we predict that LSST will discover 6–51 ISOs (with the highest yield for $q_s = 2.5$), for an assumed number density $n(H_r \leqslant 22) \sim 0.1\,\mathrm{au}^{-3}$ (K. J. Meech et al. 2017; A. Do et al. 2018); see Appendix C for the full calculation. Caution is necessary when interpreting the number of successful discoveries in LSST. The ISO discovery rate is linearly, positively correlated with the spatial number density n, which has a large uncertainty (E. G. Flekkøy & R. Toussaint 2023). Calibration of surveys for ISO detectability is challenging; it is possible that ISOs were present but not discovered. The discovery rate is also nonlinearly negatively correlated with the intrinsic absolute magnitude distribution. The result is a degeneracy, where a shallow absolute magnitude distribution slope and a high number density will produce the same number of LSST discovered ISOs as a steep absolute magnitude distribution slope and a low number density. Thus, the number of ISOs that LSST discovers will not independently constrain the luminosity function. However, the distribution of H_r values within the discovered sample may provide more information, as shown in Figure 6.

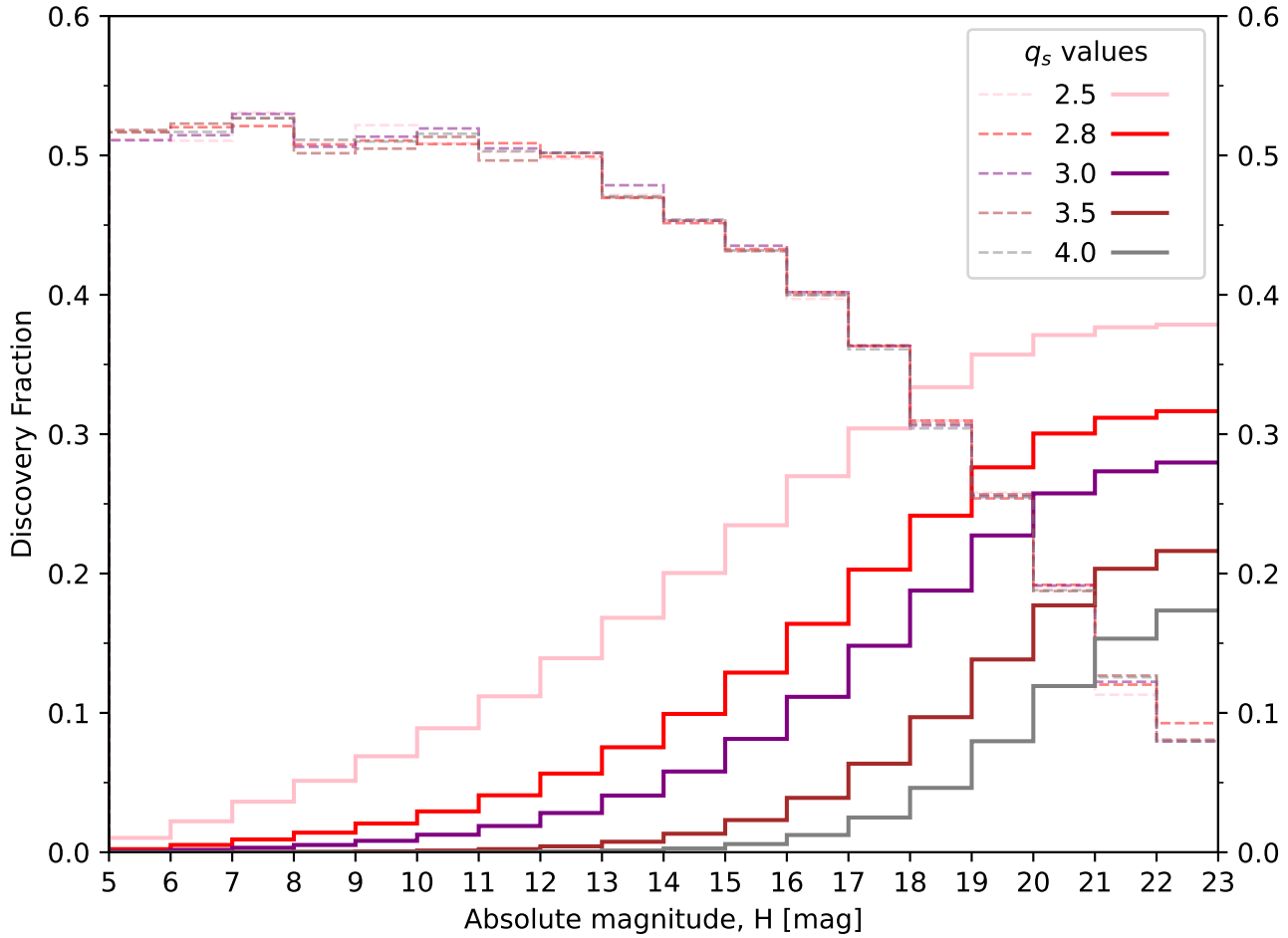

Figure 5. Discovery completeness functions for the absolute magnitude of observed ISOs in LSST per H_r interval (dashed lines) and cumulatively (solid lines). For $H_r < 13$, 50% of observed ISOs are discovered; however, this discovery rate decreases for objects with $H_r \geqslant 13$, where the lowest discovery rate is associated with the smallest objects (<10% for $H_r \geqslant 22$). Regardless of the intrinsic absolute magnitude distribution, <40% of the ISOs observed by LSST were discovered.

We investigated whether the LSST sample of ISOs could constrain the intrinsic absolute magnitude distribution by performing a power analysis. We constructed two sets of H_r values, each containing N random draws from different "models" (i.e., discovered ISO absolute magnitude distributions with different slopes q), and compared both samples to both models using an Anderson–Darling test (T. W. Anderson & D. A. Darling 1952). This process was performed for 10^3 trials. The minimum sample size N where the incorrect model is rejected over the correct model for at least 95% of trials represents the 95% confidence interval. To ensure these criteria were met for the number of trials performed, we used a conservative threshold of 95% $\pm$ 3σ where σ is the error on a binomial confidence interval. The results are presented in Table 2 and visually illustrated by Figure 7. Note that the asymmetry in Table 2 is expected due to the number of trials performed and the conservative threshold; an overall uncertainty of one discovered ISO is suitable for this work. A negative correlation exists between the number of discoveries needed and the difference in the slope values being compared. For the same slope difference Δq_s, more ISOs are needed to differentiate between two steeper slopes (e.g., $q_s = 3.5$ and $q_s = 4.0$) than two shallower slopes (e.g., $q_s = 2.5$ and $q_s = 3.0$). The smallest expected sample size from LSST is for the steepest slope, $q_s = 4.0$. From our lower estimate of six discoveries expected from LSST, the absolute magnitude distribution slope can be constrained to within less than $\pm$1.5 of the intrinsic value. In comparison, for the largest expected sample size of 51 ISOs for the shallowest slope $q_s = 2.5$, the absolute magnitude distribution slope can be constrained to within $\simeq\pm$0.3 of the intrinsic value. These outcomes suggest that the predicted LSST sample of ISOs will strongly aid the characterization of the Galactic population, regardless of the sample size.

Other characteristics of the ISOs discovered by LSST, such as perihelia, inclination, and velocity, will also help constrain the intrinsic ISO absolute magnitude distribution slope. Figure 8 demonstrates that the perihelia and inclination distributions of ISOs in LSST will depend on the intrinsic absolute magnitude distribution. For a shallower intrinsic slope $q_s = 2.5$, LSST's ISOs will have the modal perihelion $q \sim 4$ au and an equal proportion of prograde and retrograde orbits. In contrast, for the steepest slope $q_s = 4.0$, the modal perihelion will be $q \sim 1$ au, and the LSST sample will have disproportionally prograde orbits. Although LSST will have a deeper 5σ limiting magnitude than the Pan-STARRS survey in which 1I/'Oumuamua was detected ($m_r \sim 23$ compared to $\sim$21; L. Denneau et al. 2013), we find that similar-sized objects to 1I/'Oumuamua ($H_r \sim 22.4$) are unlikely to contribute to the LSST sample, with the probability $P \sim 0.01$; we can expect at most one 1I/'Oumuamua-like "asteroidal" ISO in LSST, for current spatial density estimates.

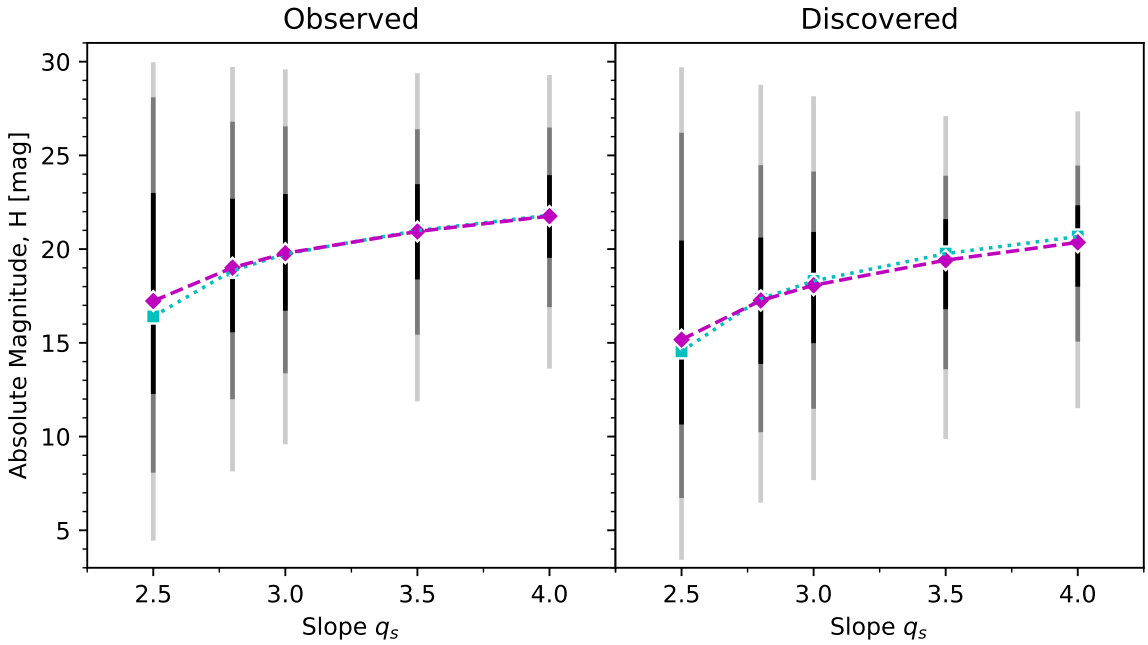

Figure 6. Summary statistics for the modeled absolute magnitude distributions of the observed (left) and discovered ISOs (right), for all considered values of slope q_s. A simple power-law function with a sigmoid rollover was fitted to each binned distribution. The resulting 1σ, 2σ, and 3σ limits for each slope q_s are indicated by vertical black lines of decreasing opacity. The mode (cyan squares) and median (magenta diamonds) values are also indicated.

Table 2
The Number of Discovered ISOs Required to Reject the Hypothesis that Their H_r Values Are Drawn from the Same Absolute Magnitude Distribution as a Given "Model" Distribution

q_s	2.5	2.8	3.0	3.5	4.0
2.5	⋯	45	21	6	4
2.8	45	⋯	174	15	8
3.0	22	173	⋯	26	11
3.5	7	16	27	⋯	74
4.0	4	8	11	73	⋯

Note. The asymmetry in values for the same comparison is expected due to the number of trials performed and the conservative threshold used.

This is an order of magnitude less probable than inactive objects of dimensions comparable to the nuclear diameter of 2I/Borisov. There is also a discernible difference in the expected median velocity at infinity for the different absolute magnitude distribution slopes. The steepest slope $q_s = 4.0$ results in slower ISOs discovered in LSST, with a median of $v_\infty \sim 35\,\mathrm{km\,s^{-1}}$ compared to $v_\infty \sim 45\,\mathrm{km\,s^{-1}}$ for the shallowest slope $q_s = 2.5$. Interestingly, both known ISOs had v_∞ consistent with steeper slopes.

The Ōtautahi–Oxford model allows us to explore several properties of the LSST ISO sample: the age of the ISOs (which in the model is held contemporaneous with the star's age, assuming an early unbinding event), the metallicity of their origin stars, and the water-mass fraction of the ISOs assuming they all formed beyond the ice line, which correlates with stellar metallicity. We see no relationship between these properties and the H_r-distribution; the LSST sample is effectively unbiased on these parameters. The ISO preencounter velocity structures predicted in M. J. Hopkins et al. (2025) from Galactic dynamical structures are also recovered for the LSST sample, in both (U, V) and (V, W) phase space, although slightly less pronounced (Figure 9). The overdensity at the Sun's velocity $(U, V, W) = (0, 0, 0)$ caused by gravitational focusing is also discernible, particularly in (U, V) space.

5. Structural Patterns in ISO Discoveries

The survey cadence and discovery choices will uniquely shape the properties of the LSST ISO sample. The orbital orientations of the LSST ISO sample will be biased due to the telescope's location and the survey footprint. The Simonyi Survey telescope is located on Cerro Pachón (Chile) in the Southern Hemisphere; as a result, the survey footprint is restricted to fields with decl. $\delta \lesssim 35°$. This means that most ISOs with perihelia in the Northern Hemisphere will be outside of the survey footprint when they are at their brightest. The argument of perihelion and R.A. of the ascending node distributions for the LSST sample demonstrate the significance of this Southern Hemisphere survey bias (Figure 10). Orbits with $60 \lesssim \omega \lesssim 165°$ or $\Omega \sim 270°$ are distinctly underrepresented in the LSST sample compared to the Ōtautahi–Oxford model. Interestingly, 1I/'Oumuamua and 2I/Borisov have arguments of perihelia near the peak probable value of LSST discoveries.

The discovery circumstances of ISOs in LSST will be contrary to expectations for other solar system small body populations. Previous modeling efforts have shown that most LSST discoveries of bound solar system objects are made in the first few years of the survey (S. Eggl et al. 2019). A similar prediction could be naively applied to ISOs; when LSST reaches first light, it might first discover the ISOs in the initial observable survey volume, until an equilibrium discovery rate is reached when the refreshing of the local ISO population from more distant points becomes the dominant driver of the discovery rate. However, our simulations demonstrate that ISOs will be discovered at an almost constant rate throughout the survey (Figure 11). We also investigated whether there was a correlation between seasonal effects (e.g., solar conjunction,

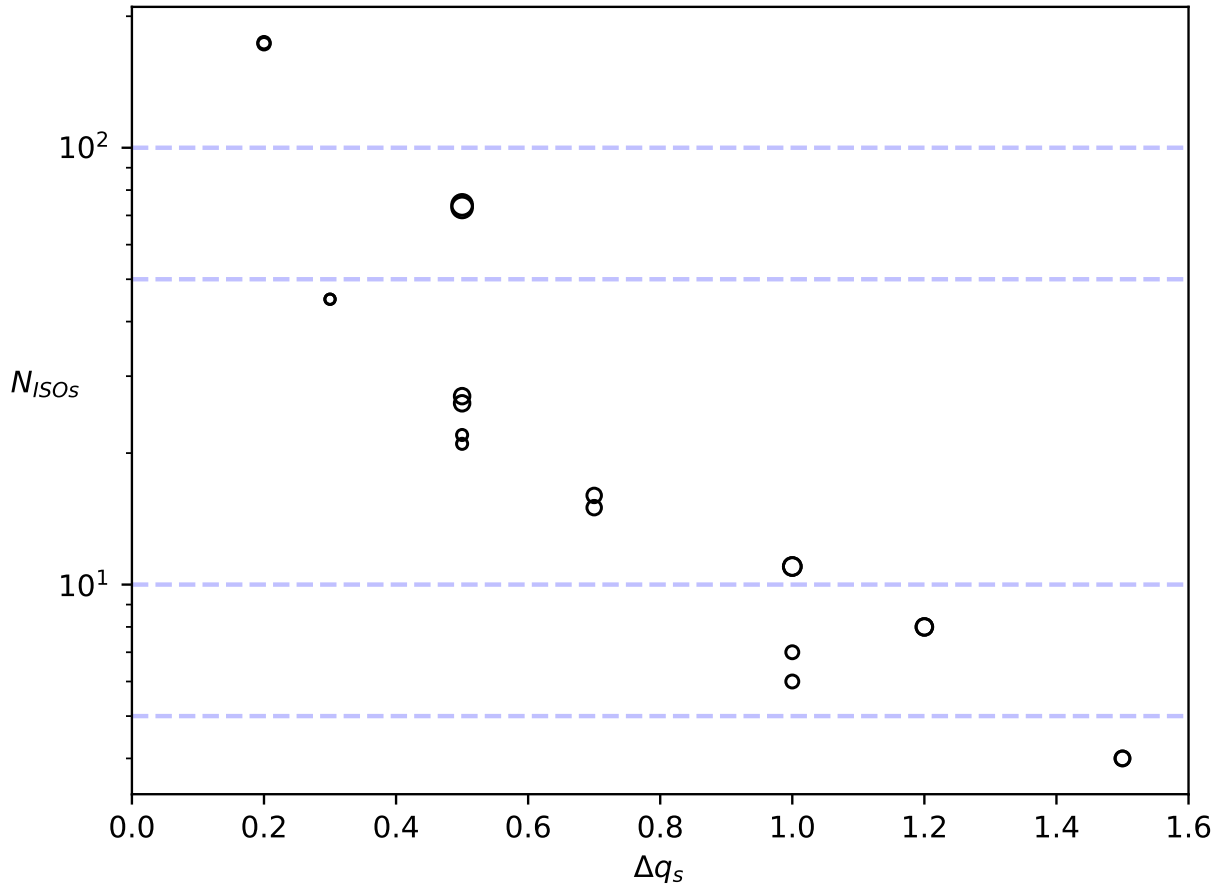

Figure 7. Comparison of the difference in slope q_s of the two compared model H_r distributions to the number of discoveries required to reject models. The blue horizontal dashed lines indicate sample sizes of 5, 10, 50, and 100 ISOs. Fewer discovered ISOs are needed to distinguish between slope values that are further apart. The size of each data point is proportional to the product of the compared slope values: for the same Δq_s, steeper slopes require more discoveries in order to be distinguished.

annual weather patterns, etc.) and the discovery rate of ISOs. We found that interyearly ISO discoveries are also uniformly distributed in time, accounting for leap years and regularly scheduled maintenance downtime of a variable length. Thus, we interpret the linear discovery of ISOs in LSST as a consequence of the assumed uniform refresh rate of ISOs entering and leaving their observable sphere, rather than specific cadence choices or annual Sun–Earth geometries. Additionally, ISOs will be discovered before and after perihelion with equal probability (Figure 11); however, the most probable scenario is discovery ∼20 days after perihelion for all slopes q_s. This contradicts previous predictions that ISOs will be predominantly discovered preperihelion (D. J. Hoover et al. 2022).

Contrary to expectation (e.g., M. E. Schwamb et al. 2023), the twilight microsurvey does not provide critical discovery of asteroidal ISOs. Our simulations show that ISOs discovered only in the twilight survey typically have absolute magnitudes $17 \leqslant H_r \leqslant 20$ with preferentially lower perihelia and velocities at infinity than objects discovered in the main survey. In all other characteristics considered in this work (both orbital and physical), twilight discovered ISOs are consistent with objects found in the main survey. In reality, the twilight ISO discoveries make up 0.9%–1.4% of all discoveries for any slope q_s, and a further 0.3%–2.2% of discovered ISOs are found by both the twilight and main surveys. Thus, for our predicted number of LSST ISOs, we can expect at most one ISO discovery from the twilight survey (with ∼70% probability) and about one object discovered in both surveys, which occurs for the shallowest absolute magnitude slope $q_s = 2.5$. For all twilight discoveries, ∼54%−65% are discovered in evening twilight, with the slope $q_s = 2.5$ incurring the highest proportion of morning twilight discoveries.

Our simulations suggest that ISOs will be discovered at small distances and velocities. ISOs found in the main survey typically have heliocentric distances $r_h \sim 1-3$ au, geocentric distances $\Delta \sim 0-3$ au, and on-sky rates of motion $\mu \sim 0°-2°\,\mathrm{day}^{-1}$ at discovery (Figure 12). This is broadly consistent with previous results from N. V. Cook et al. (2016) and D. J. Hoover et al. (2022), which predicted that ISOs would be discovered with perihelia $q \approx 1$ au (contrast Figure 8) and pass within ∼1.5 au of the Earth. The distributions of distance and velocity at discovery for our simulated Ōtautahi–Oxford ISOs also place into context the nature of the first ISO; 1I/'Oumuamua was discovered comparably close to Earth ($\Delta \sim 0.2$ au, but in a shallower survey), although with an atypically large on-sky rate of motion ($\mu \sim 6°\,\mathrm{day}^{-1}$). While most ISOs discovered by LSST will be found near the Earth, only a minority will be discovered with motion rates as extreme as 1I/'Oumuamua. For instance, ⩽0.05% of discovered ISOs will have an on-sky motion faster than the LSST SSP threshold of $10°\,\mathrm{day}^{-1}$. The distributions of distance and velocity at discovery are also

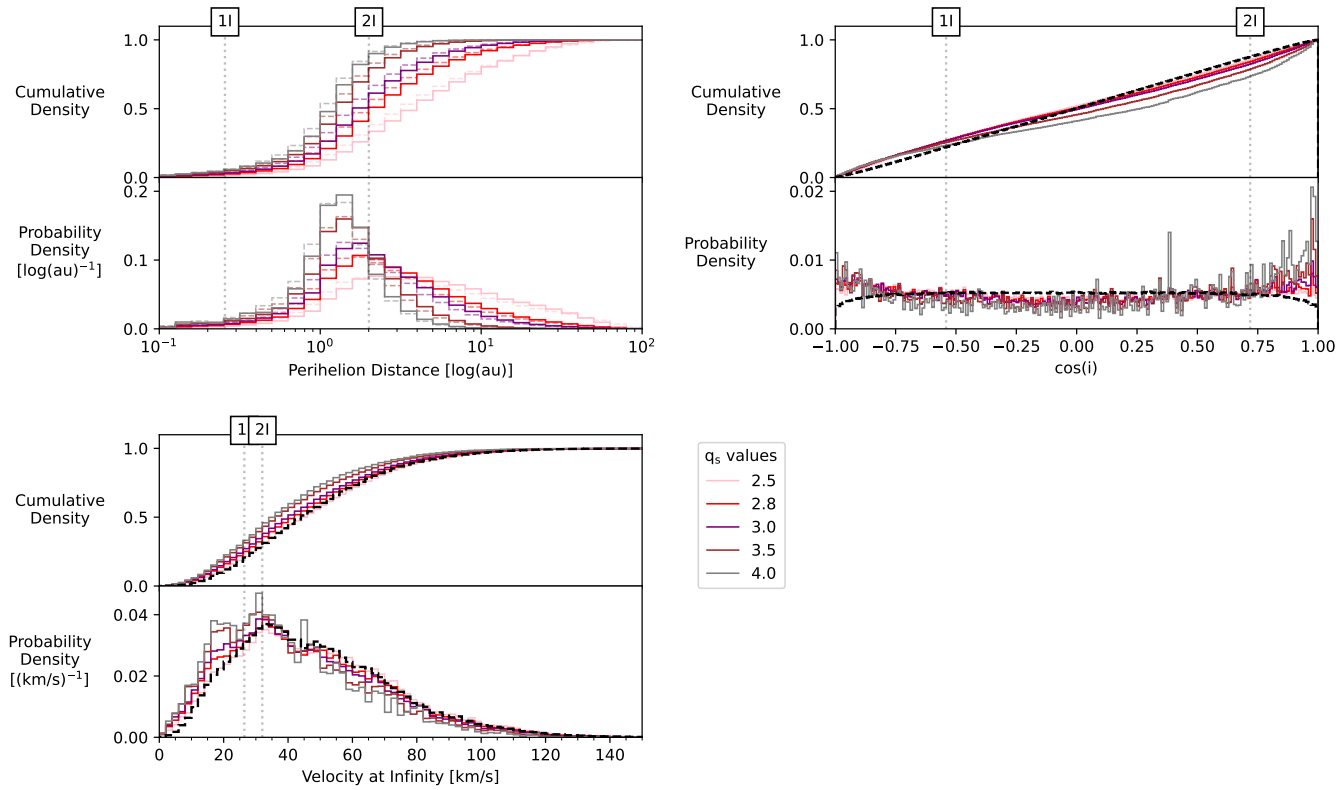

Figure 8. Cumulative and probability density functions for the perihelion (top left), cosine of inclination (top right), and velocity at infinity (bottom) for ISOs discovered in LSST. Comparisons are made to the observed ISO sample (colored dashed curves) for perihelion and the Ōtautahi–Oxford model (black dashed curve) for inclination and velocity. Vertical dotted black lines indicate the corresponding values for the two known ISOs.

dependent on the intrinsic absolute magnitude distribution. Objects from a steeper slope distribution are typically discovered at lower heliocentric and geocentric distances and higher on-sky velocities than from a shallow slope distribution.

The most probable r-band apparent magnitude of ISOs at discovery is ∼23.3 mag, in agreement with our prediction (see Section 3.1). Above this value, the likelihood of discovery decreases rapidly with m_r; no ISOs are discovered with an apparent magnitude $m_r \geqslant 25$. The modal discovery magnitude of ISOs in LSST is ∼4.5 mag fainter than the apparent magnitudes of the two known ISOs at their respective discoveries (Figure 12), as expected given the larger-aperture facility. In conjunction with the distances of ISOs at discovery, this confirms that LSST will find ISOs within a larger detectable volume than previous surveys.

In addition to the observation scheduling within the LSST footprint, the intrinsic dynamics of the Galactic ISO population affect the on-sky location of an ISO observed by LSST. In general, the on-sky motion of ISOs in LSST is from north to south; from the Galactic plane inward of the solar circle to the Galactic plane outward of the solar circle. At the first observation, ISOs tend to be found in the northern area of the LSST footprint, nearest to the solar apex (Figure 13), particularly concentrated in the northernmost rolling stripe. The solar apex is the direction of motion of the Sun relative to the local standard of rest (R. Schönrich et al. 2010), located at approximately $(\alpha, \delta) = (18^{\rm h}, +30^{\circ})$ in the northern celestial hemisphere (I. Ridpath 2012). This is the direction from which ISOs are expected to encounter the solar system (T. A. McGlynn & R. D. Chapman 1989; S. A. Stern 1990); see Figure 1. Compared to their first observation, ISOs are then discovered almost uniformly across the LSST footprint. The majority of discovered ISOs (95%) have an arc length in LSST $\geqslant$4–17 days (median of 35–200 days); the steepest absolute magnitude slope $q = 4.0$ has the shortest visibility. Their last observation is most likely nearest the solar antapex (Figure 13), typically $\geqslant$10 days after their first observation in LSST for 95% of ISOs from the $q_s = 2.8$ distribution and $\geqslant$100 days for 50% of discoveries.

The rolling cadence strategy within the survey causes distinct patterns in the LSST ISO discoveries. While most ISOs are discovered within ∼100 days of their first observation in LSST, some ISOs are found over a year later (Figure 14). The probability of discovery at >100 days after an initial detection also appears to oscillate in log space over 1 yr, reaching maxima at $\sim 365n + 15$ days after the first detection (where n is an integer number of years after survey start, and 15 days is the maximum length of the moving object discovery window—see Section 3.2). This is a result of the rolling cadence strategy; an object may be observed in an "off" stripe in 1 yr but is insufficiently sampled to be discovered and is subsequently discovered by LSST the following year once the stripe rolls "on". Figure 15 demonstrates this within the context of the LSST footprint. ISOs discovered in rolling years are first observed across several areas on the celestial sphere; i.e., they are not necessarily constrained to being observed and discovered in one stripe only. Additionally, ISOs are slightly more discoverable in odd rolling years than even rolling years. This is due to odd years surveying the more northern rolling stripe pattern. Examining a random selection of ISO on-sky trajectories from their first, discovery, and last observations shows that, despite the general on-sky motion of

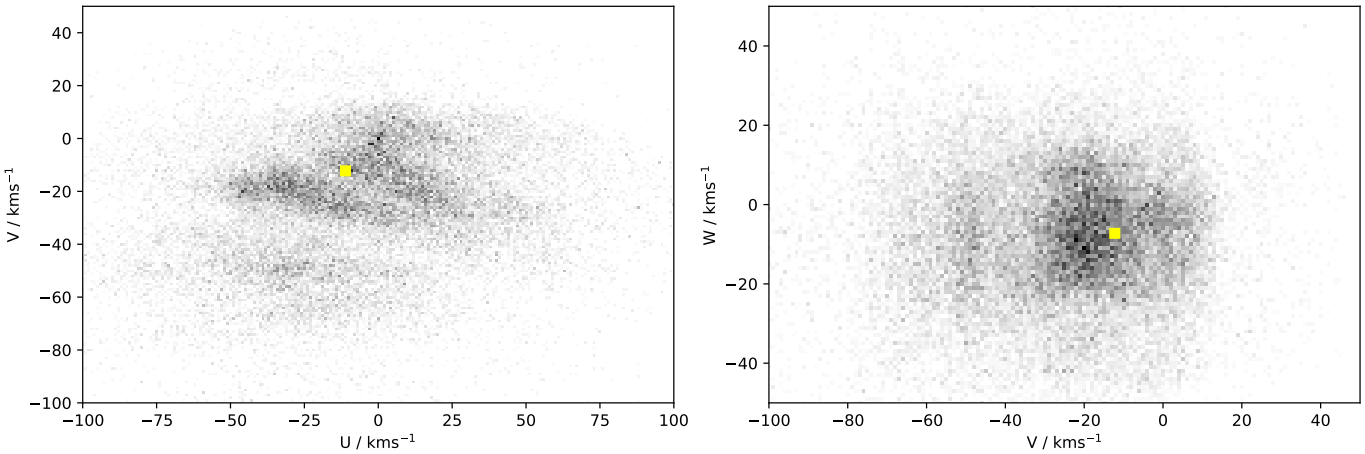

Figure 9. Probability density functions for the Galactic velocity distributions of the LSST discovered ISOs from the $q_s = 2.8$ intrinsic absolute magnitude distribution. The gray scale is normalized such that the sum of all (U, V) or (V, W) cell of probability density is equal to 1; the darkest cells are the most probable. The yellow square denotes the local standard of rest. The structures predicted by M. J. Hopkins et al. (2025) are still apparent in the velocity distribution the discovered ISOs will be drawn from, including the overdensity at the Sun's velocity (U, V, W) = (0, 0, 0) due to gravitational focusing; this is less discernible in (V, W) than (U, V) due to being washed out in the distribution marginalized over U.

ISOs from north to south, some ISOs have an on-sky motion in the opposite direction.

6. Characterizing LSST's ISOs with Follow-up

After their discovery in LSST, ISOs will be a high priority for follow-up characterization. While LSST will provide some incidental self-follow-up, there is limited capacity for ISO-targeted observations by the Simonyi Survey Telescope (I. Andreoni et al. 2024). Instead, the responsibility of ISO follow-up will fall on telescope facilities around the world. Observational campaigns requesting telescope resources typically take hours to days (for Director's Discretionary time) to months (for regular semester time) to be approved, so it is critical to know whether the target ISO will have reduced in brightness by the time the observations are approved and scheduled.

We investigate the length of time after discovery that an LSST-discovered ISO will be bright enough to be targeted by various facilities. We use two indicative magnitude limits: $m_r = 23$ for colors or spectroscopic instruments (e.g., Gemini Multi-Object Spectrograph at Gemini Observatory; E. Dotto et al. 2003)[11] and $m_r = 28$ mag for space telescopes (e.g., Hubble Space Telescope; M. Marinelli & L. Dressel 2024). Since an ISO will generally have an initial multiday arc from its discovery images (single-day arcs are limited to the small fraction of twilight survey discoveries), we assume that the object's on-sky velocity would be known throughout the rest of its passage through the solar system to a level of accuracy suitable for nonsidereal observations with small-FOV instruments. Therefore, we ignore trailing losses in the following analysis. For the rest of this section, an ISO's "apparent magnitude" refers to its untrailed apparent magnitude within a nonsidereally tracked follow-up context, unless stated otherwise.

Due to the time-bounded nature of surveys, when LSST begins surveying, some ISOs will already be outbound from the solar system while others are just on their way into their observable sphere. This means that the ISO discoveries in the earliest survey years of LSST are a combination of objects eventually reaching an observable magnitude and objects that would have been discovered already if the survey had started earlier. This phenomenon is both orbit- and luminosity-function dependent, as the amount of time an object spends at a magnitude observable by LSST is related to its perihelion distance and absolute magnitude. The largest objects ($H_r = 5$) can have residence times on the order of decades, thus contributing to this effect. However, these are also far less frequent in the intrinsic and discovered populations (regardless of the absolute magnitude distribution chosen in this work), so the impact should be minor. Nevertheless, we analyze only ISO discoveries from Year 2 to Year 6 within the simulated 10 yr survey to mitigate this as much as possible. For each discovered ISO, we evaluate its apparent magnitude until it becomes fainter than $m_r = 28$ mag. Additionally, we only consider objects from the $q_s = 2.8$ absolute magnitude distribution for the following analysis.

Most ISOs are discovered already bright enough for spectroscopic observations. This is H_r dependent; as H_r increases, the proportion of objects that never or eventually brighten to $m_r = 23$ after their discovery decreases roughly linearly. Objects are discovered above and below the $m_r = 23$ limit due to differences in their orbital position relative to the perihelion passage. As expected, most objects fainter than $m_r = 23$ at discovery are on inbound trajectories, while those that are never brighter than $m_r = 23$ after discovery are on outbound trajectories. Objects brighter than $m_r = 23$ at discovery are equally likely to be on the inbound or outbound portion of their orbit. Smaller ISOs ($H_r \geqslant 17$) are almost always discovered brighter than the $m_r = 23$ threshold. As a result, 93.4% of the discovered ISOs will be initially brighter than $m_r = 23$, while 4.0% and 2.7% never or eventually reach this magnitude after their discovery, respectively. Of the ISOs bright enough for spectroscopic observations immediately, 95% will be observable for $\geqslant$25 days (Figure 16); this is also true for the most probable discovered ISO with $17 \leqslant H \leqslant 18$. Inbound objects are observable $\sim$2–3 times longer than outbound objects; the longest observability period for the 95% percentile is $\geqslant$1105 days compared to $\geqslant$459 days (Figure 17).

All ISOs are brighter than the magnitude limit $m_r = 28$ for space-based telescope follow-up for at least 30 days after their discovery. Most (95%) will be viable for follow-up for

[11] For instance, 1I/'Oumuamua was predicted to have $m_r = 22.7$ during the observations in M. T. Bannister et al. (2017).

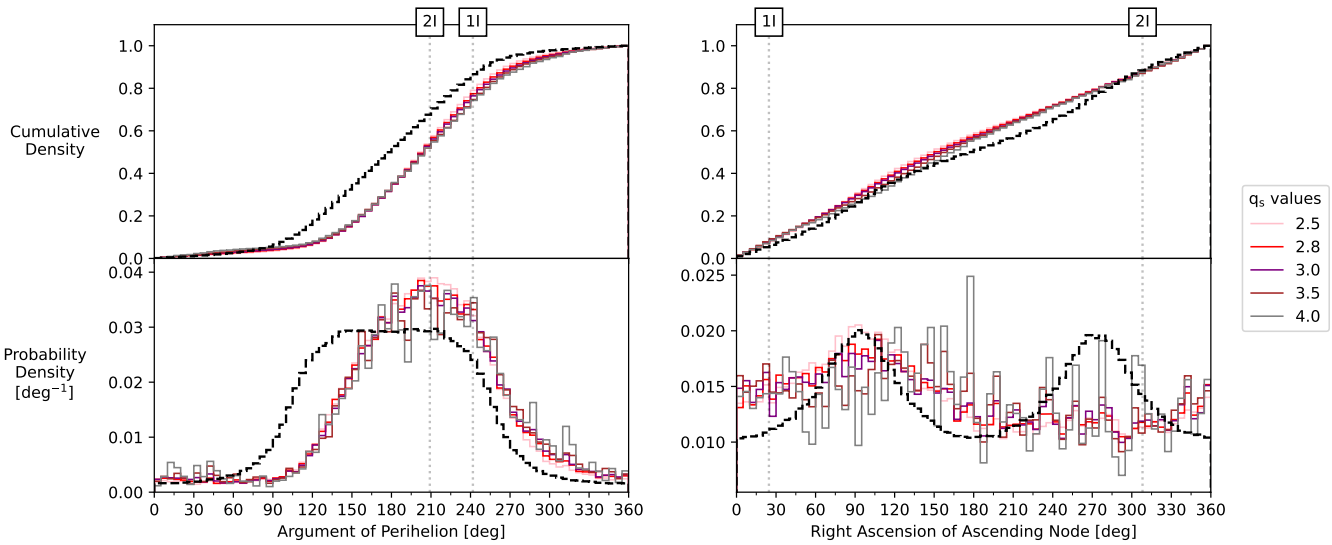

Figure 10. Same as Figure 8, but for argument of perihelion (left) and R.A. of the ascending node (right). The dashed black curves indicate the cumulative and probability density functions for the intrinsic model (the Ōtautahi–Oxford population).

$\geqslant$160 days; this increases to $\geqslant$199 days for the most probable discovery ($17 \leqslant H \leqslant 18$). In rare cases (95th percentile), ISOs are observable for $\geqslant$3084 days, or $\sim$8.5 yr. Inbound objects are observable $\sim$1.2−1.6 times longer than outbound objects; the longest observability period for the 95th percentile is $\geqslant$3503 days compared to $\geqslant$2434 days ($\sim$9.5 yr and $\sim$6.5 yr, respectively).

7. Discussion

ISOs are a cosmogonically unique and observationally disadvantaged small body population. While they may hold the answers to many questions about the fundamental physics of planet formation, they are rarely discovered. In this survey simulation of ISOs in the upcoming LSST, we quantify the observational and discovery biases for the Ōtautahi–Oxford population model, under realistic assumptions about ISO physical properties. From our simulated discovery rate of ISOs in LSST, we estimate that 6–51 ISOs will be discovered during LSST. This is in agreement with works such as N. V. Cook et al. (2016) and D. E. Trilling et al. (2017), and is lower than other studies, which omit trailing losses, LSST cadence details, and/or LSST SSP discovery criteria (M. Rice & G. Laughlin 2019; D. J. Hoover et al. 2022; D. Marčeta & D. Z. Seligman 2023). The number of discoveries we expect is also sufficient to test the prediction of M. J. Hopkins et al. (2025) that the Ōtautahi–Oxford model we use here will be distinguishable ($N = 20$ for 2σ or $N = 50$ for 3σ difference) from OB-type smooth Gaussians (see Figure 9).

7.1. The Unobservability of ISOs: A One-in-a-million Detection

ISOs are extremely difficult to observe and discover in solar system surveys such as LSST due to a unique array of observational biases. In the same 10 yr in which the LSST discovers the 6–51 we predict above, a monumental $\sim 10^7$ ISOs with $H_r \leqslant 23$ will pass within 100 au of the Sun. Thus, the term "discovery completeness" for ISOs is highly impractical; $\lesssim 3.4 \times 10^{-4}$% of the ISOs that intersect the 100 au radius sphere in our simulations are discovered by LSST.

A fundamental and invariable characteristic of ISOs is their single perihelion passage through the solar system. Unlike the majority of solar system small body populations, ISO discovery does not have the luxury of repeated attempts; like long-period comets, their single passage is the only opportunity to detect them. In addition to their single passage, an ISO's path within its observable sphere plays an important role in its discovery. The size of an ISO's heliocentric observable sphere depends on its absolute magnitude and the limiting magnitude of LSST. For an ISO to be observable by LSST, the object must have a perihelion distance within this sphere, i.e., $q \leqslant r_{\rm sph}$ (Equation (3)). The most probable perihelion for an observable ISO is $q \approx r_{\rm sph}$ rather than $q \ll r_{\rm sph}$; therefore, the amount of time an ISO spends observable and the number of observations it receives are likely small. This is confirmed by the orbital parameters of the discovered ISOs (Section 4). ISOs are most likely to be discovered in the main survey with four to six tracklets (depending on the intrinsic absolute magnitude distribution), which is almost the minimum requirement for discovery (Section 3.2). Discovered ISOs tend to have lower velocities than the model population (Figure 8), in agreement with N. V. Cook et al. (2016), and higher residence times compared to the intrinsic population, which allows them to remain observable long enough to be discoverable. This introduces an inclination bias, as prograde orbits have longer residence times than retrograde orbits of a similar orientation and shape. Our analysis agrees with the expectation of N. V. Cook et al. (2016); to the first order, the inclination of LSST's ISOs will be uniform. However, our simulations predict a bias toward prograde orbits, which increases with absolute magnitude slope (Figure 8). This is contrary to the finding of D. Marčeta & B. Novaković (2020) that LSST will be biased toward retrograde orbits, potentially due to our accounting for trailing losses, survey cadence, and moving object discovery criteria.

At least 50% of ISOs will be discovered with perihelia $q \leqslant 5$ au for absolute magnitude distributions with a slope $q_s \geqslant 2.5$ (Figure 8). This means a significant fraction of ISOs may also be discovered with perihelia beyond Jupiter's orbit. N. V. Cook et al. (2016) and D. J. Hoover et al. (2022) predicted that ISOs will be discovered with perihelia $q \approx 1$ au and pass within $\sim$1.5 au of the Earth. Our simulations disagree; ISOs with perihelia $q > 2.5$ au will make up 10%−70% of LSST

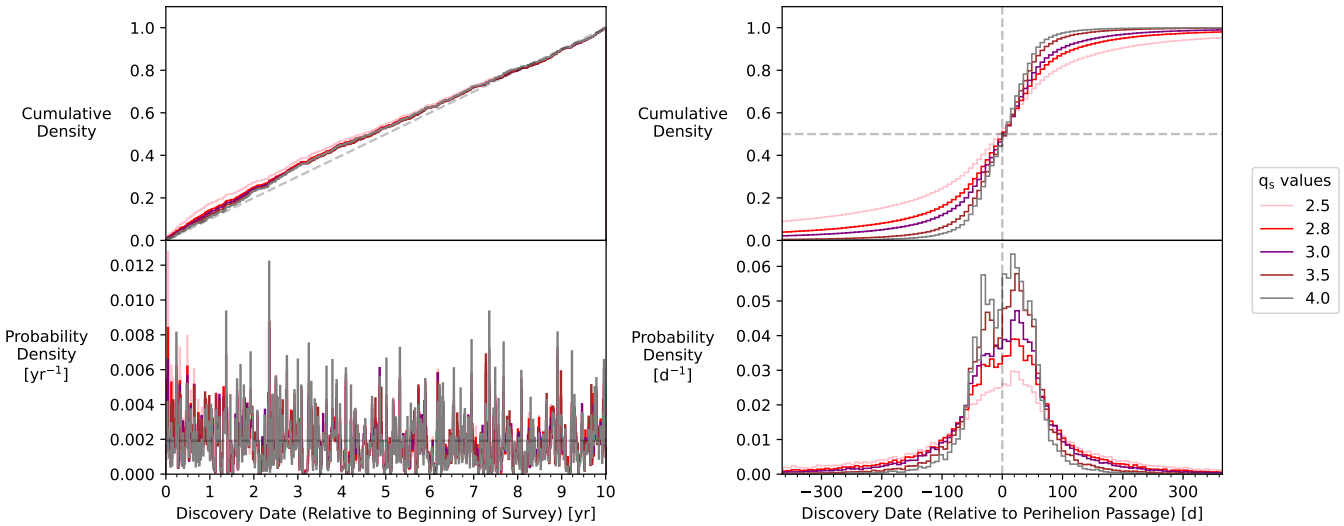

Figure 11. Same as Figure 8, but for discovery date relative to the start of the survey (left) and to the time of perihelion passage (right). The dashed lines indicate a uniform discovery rate (left), the time of perihelion passage (right; vertical line), and the 50% cumulative density (right; horizontal line).

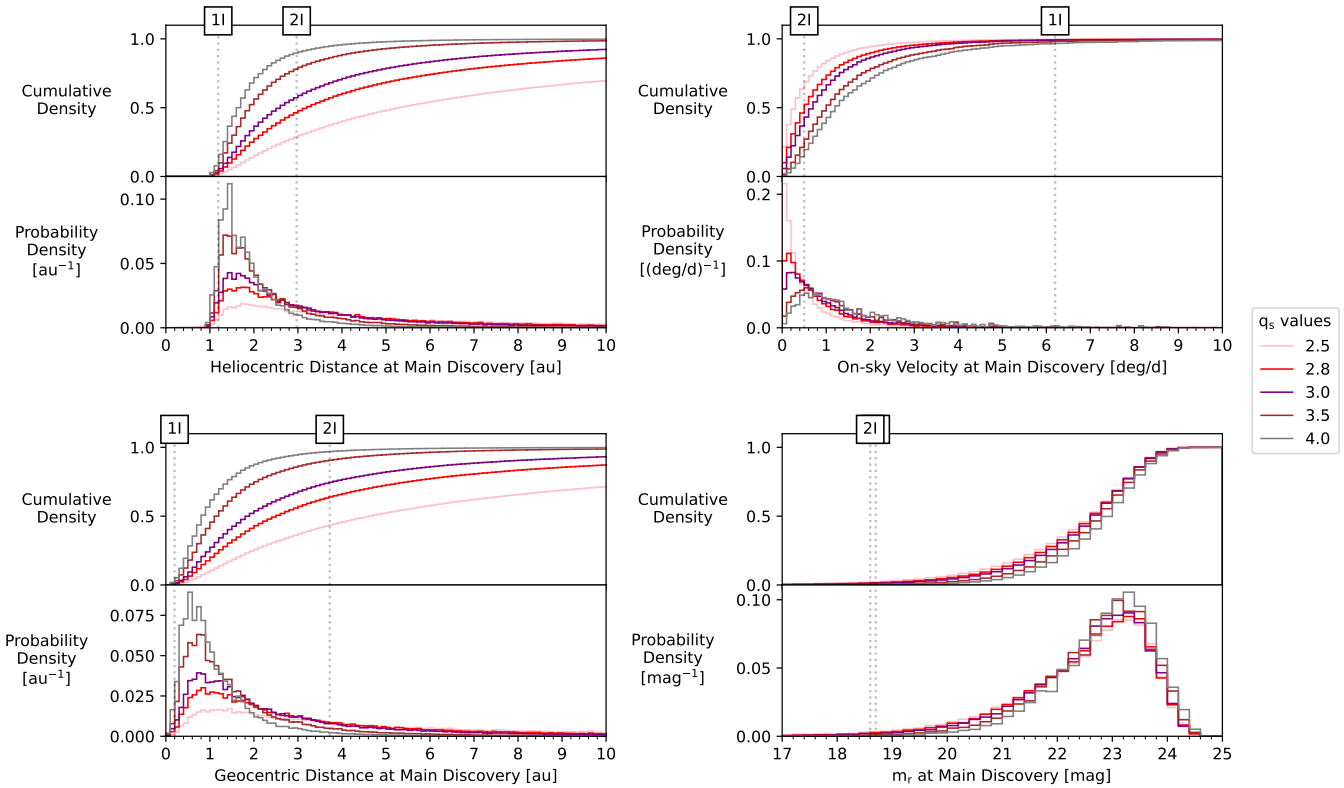

Figure 12. Same as Figure 8, but for the properties of ISOs at the time of their discovery in the main survey of LSST. Top left to bottom right: heliocentric distance, on-sky velocity, geocentric distance, and apparent r-band magnitude m_r. Vertical dotted black lines indicate the corresponding values for the two known ISOs at the time of their discovery; note that 1I/'Oumuamua was discovered by NEO discovery survey Pan-STARRS, while 2I/Borisov was discovered at low solar elongation and was cometary.

discoveries, depending on the absolute magnitude distribution. The median H_r of our discoveries ranges from 15.2 to 20.4 mag for $2.5 \leqslant q_s \leqslant 4.0$ (Figure 6). Assuming an example albedo of $p = 0.05$, this corresponds to objects of a diameter $D \sim 0.5$–5.4 km. This is larger than the mean ISO size predicted by D. Marčeta & D. Z. Seligman (2023); however, their discovery criteria only required three observations for an object to be discovered.

Other factors that we do not model in this work may also impact the observability of ISOs in LSST. One known observational bias for at least some of the ISO population is due to light-curve variability. 1I/'Oumuamua, the only asteroidal ISO discovered so far, demonstrated extreme fluctuations in brightness due to its shape and rotation rate ('Oumuamua ISSI Team et al. 2019), which impacted its observability (W. G. Levine & R. Jedicke 2023). While the implementation

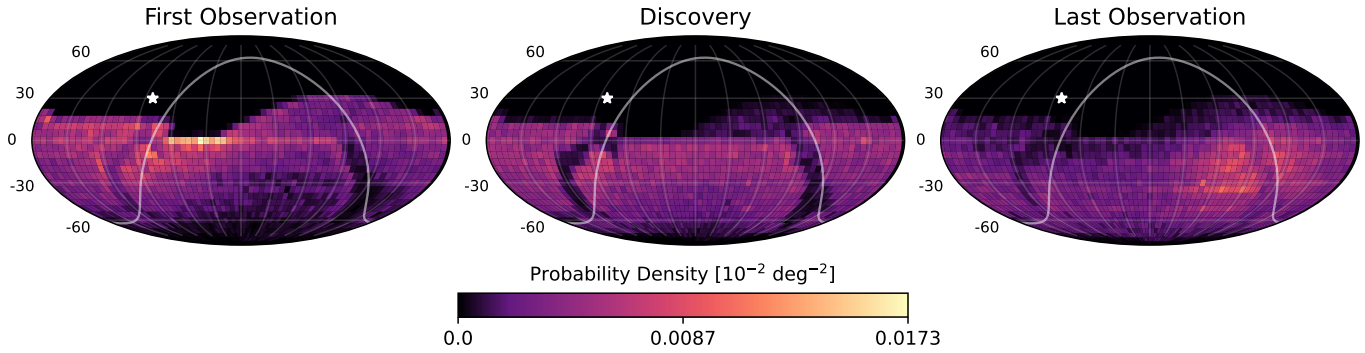

Figure 13. Two-dimensional illustrations for the on-sky locations (α, δ) for the first, discovery, and last images of the LSST discoveries for $q_s = 2.8$ for all years of the survey. R.A. α increases to the right in each projection, from $-180°$ to $180°$. The white star indicates the solar apex, and the thin white line indicates the Galactic plane. Other absolute magnitude slopes also show similar trends.

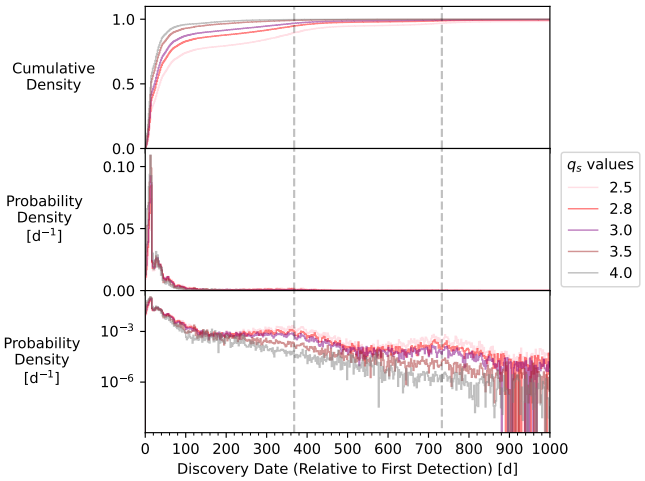

Figure 14. Same as Figure 8, but for discovery date relative to first detection. The dashed gray vertical lines indicate 380 and 745 days, respectively, corresponding to integer years plus 15 days.

of an ISO population shape model is left for future work, preliminary simulations of 1I/'Oumuamua-like objects—which we parameterize with an absolute magnitude $22 \leqslant H_r \leqslant 23$, axis ratio a:b:c = 6:1:1, and rotation period $P \sim 8.7$ hr—within our modeling framework— are ∼20%−40% less discoverable in LSST than spherical objects (a:b = 1:1) of a comparable size, for slopes $2.5 \leqslant q_s \leqslant 4.0$. This suggests that if a correlation exists between shape and size in the intrinsic ISO population, the discoverability of small ISOs may be more greatly impacted than that of larger ISOs.

Given that ISOs are almost always bright enough for characterization observations immediately following discovery in LSST, and this holds regardless of whether the ISO is inbound or postperihelion, it remains reasonable to have target of opportunity programs in reserve at major facilities. Immediate diagnosis of any unusual properties will remain a high priority, especially given the sample is likely to be a few tens in number. However, after initial characterization, the duration of observability is long enough that many ISOs may be accommodated within regular Time Allocation Committee cycles—ideally, this would be with multisemester scheduling continuity.

7.2. ISOs from the Perspective of a Southern Telescope

The location of the Simonyi Survey Telescope in the Southern Hemisphere limits the amount of Northern Hemisphere on-sky area included in the survey footprint; in particular, the solar apex lies ∼10° outside of the LSST footprint. Thus, it is expected that the ISOs discovered in LSST will be a biased sampling of the intrinsic Ōtautahi–Oxford model. Our quantification of the discovery biases on ISO discovery in LSST demonstrates the losses incurred from surveying a dominantly Northern-inbound small body population with a dominantly Southern-pointing telescope. Orbits discovered in LSST are generally oriented with their perihelia in the Southern Hemisphere (Figure 10). In contrast to previous expectations that ISOs will be found preperihelion (D. J. Hoover et al. 2022), our simulations show that ISOs are equally likely to be discovered preperihelion as postperihelion by LSST (Figure 11) and are discovered almost uniformly across the LSST footprint (Figure 13). Even so, ISOs are more likely to be first discovered in LSST near the Galactic plane interior to the solar circle. This confirms that most ISOs encounter the solar system from the direction of the solar apex, and suggests that inbound ISOs would be more discoverable in a Northern Hemisphere survey of equivalent limiting magnitude to LSST.

7.3. Potential Improvements to LSST's ISO Discovery

The LSST SSP discovery criteria affect the possible ISO discoveries in LSST. The current moving object discovery requirements are three tracklets on different nights within 15 days. These criteria result in the discovery of ∼15%−40% of all observed objects, depending on the absolute magnitude distribution. However, additional simulations for $q_s = 2.8$ easing the three-tracklet requirement to two tracklets on two nights within the same period increased the discovery completeness of observed ISOs from ∼34% to ∼50%. As we find the number of tracklets per object depends on the absolute magnitude distribution of the population (Section 4), this may have a greater impact on an ISO population with a steeper slope q_s.

Realistically, reducing the ISO discovery criteria to require fewer images would decrease the computational accuracy and efficiency. To the first order, moving objects are discovered by attempting to fit orbits to multiple tracklets and identifying the associated error (G. Bernstein & B. Khushalani 2000). This is extremely computationally expensive, but recent advances in object detection have shown reductions in this cost. For example, the LSST SSP will use HelioLinc (M. J. Holman et al. 2018) to cluster predetermined tracklets in a heliocentric frame and link them. Other methods include a shift-and-stack approach (e.g., W. C. Fraser 2024; W. C. Fraser et al. 2024) or tracklet-less linking algorithms (e.g., J. Moeyens et al. 2021). Both methods have their advantages, but both may be

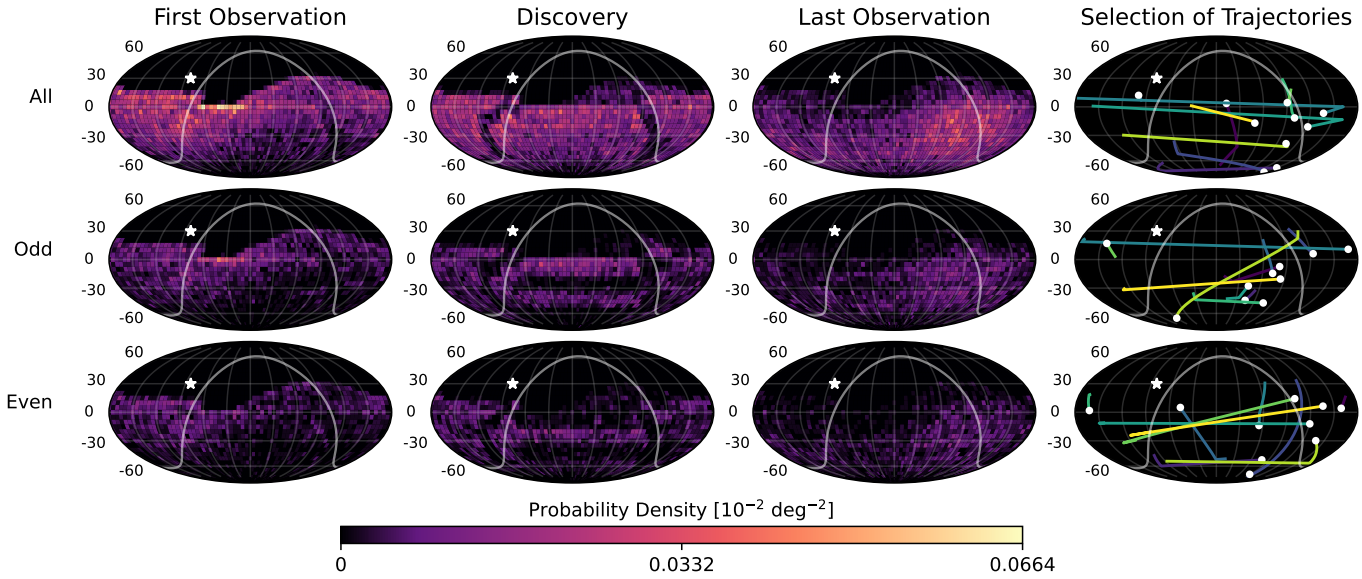

Figure 15. Two-dimensional illustrations for the on-sky locations (α, δ) for the first, discovery, and last images of the LSST discoveries with $13 \leqslant H \leqslant 14$ for $q_s = 2.8$ for all years (top row), odd rolling years (middle row), and even rolling years (bottom row). This excludes ISOs discovered in Year 2 of the simulation, which only deploys a rolling cadence over half of the survey footprint. R.A. α increases to the right in each projection, from –180° to 180°. The white star indicates the solar apex, and the thin white line indicates the Galactic plane. The last column shows the set of observations (first, discovery, last) for 10 randomly selected discovered ISOs. The observations are connected by straight lines of random color, which may appear curved due to the spherical projection, and the last observation is marked by a white dot to indicate the ultimate direction of motion.

challenged by the low observation count and wide-ranging on-sky distribution and motion rate of ISOs. Undoubtedly, without the constraint of extra observations, moving object detection algorithms will struggle to perform without high false-positive rates. However, we find that a small number of undiscovered ISOs may be recoverable from simply linking objects across visits in the LSST Deep Drilling Fields, which suggests that there may be additional methods of ISO discovery in the LSST data set beyond the LSST SSP pipeline.

7.4. Missions to ISOs

Since the discovery of 1I/'Oumuamua and 2I/Borisov, the possibility of an ISO space mission has been raised. ESA's upcoming Comet Interceptor mission is an obvious choice for an ISO flyby. The mission design of Comet Interceptor to wait in the Sun–Earth L2 point until an appropriate target is identified (G. H. Jones et al. 2024) is optimal for the uncertainty of when the next ISO will pass through the solar system. However, as an F-class ESA mission Comet Interceptor has a restricted Δv budget to maneuver to its target from the L2 position (J. P. Sánchez et al. 2021), so target selection is critical to the mission's success. Eligible targets must pass close to the Earth's orbit ($0.85 \leqslant r_{\rm h} \leqslant 1.35$ au) near their ascending or descending node (to minimize out-of-plane Δv costs), with relative flyby speeds up to $\sim$70 km s^{-1}. Our analysis shows that $\leqslant$0.95% of the ISOs discovered in LSST will reach a heliocentric distance accessible to Comet Interceptor, i.e., have perihelia $q \leqslant 1.35$ au (Figure 8). A mission with a larger Δv budget would likely have greater opportunity and capability for an ISO flyby.

Recent studies have suggested different strategies for ISO missions. S. A. Stern et al. (2024) recommended a storage-in-orbit approach with the budget $\Delta v \sim 4.0$ km s^{-1}. However, the mission requires up to $\sim$40 days for the Earth and Moon to align to the optimal orientation for an Earth swing by and the spacecraft to exit the Earth–Moon L1 storage position before an $\sim$90 day travel time until target interception. For a similar design, D. Landau et al. (2023) estimated that $\sim$40% of ISOs within 10 au of the Sun would be accessible for a rendezvous mission. D. Seligman & G. Laughlin (2018) explored a different strategy: a kinetic impactor producing a plume of internal materials to be analyzed, similar to NASA's Double Asteroid Redirection Test (A. S. Rivkin & A. F. Cheng 2023) and Deep Impact (M. F. A'Hearn et al. 2005) missions.

For all of the mission concepts described above, one of the key drivers for their success is the amount of planning or maneuver time available between an ISO's discovery and its intercept. We show that, even if ISOs are discovered before perihelion ($\sim$50% probability; Figure 11), the majority are found by LSST only 60–360 days beforehand (dependent on absolute magnitude slope). Depending on their trajectory relative to the Earth, some of these may be accessible within the 90 day example flight scenario proposed by S. A. Stern et al. (2024).

7.5. Implications for LSST's Cometary ISOs

While the observability of cometary ISOs in LSST, particularly the selection of a cometary activity model, is left for future work, predictions can be made qualitatively by extrapolation. Several physical differences between asteroids and comets include their absolute magnitude distribution (B. Boe et al. 2019), colors (D. Jewitt 2015), phase function (N. N. Kiselev & G. P. Chernova 1981; C. Snodgrass et al. 2011), and heliocentric brightening (D. Jewitt & H. H. Hsieh 2022). Our analysis has investigated the correlations between observability in LSST for all but one of these characteristics. The last, heliocentric brightening, is due to the evolution of the comet's coma throughout its perihelion passage. A coma increases the brightness of a comet as it moves closer to the Sun due to the increase in the sublimation rate (a function of temperature), scattering of solar light off dust in the coma, and the apparent on-sky extent of the coma relative to the observer (D. Jewitt & H. H. Hsieh 2022). Comets are anticipated to be discovered in LSST at least 5 yr

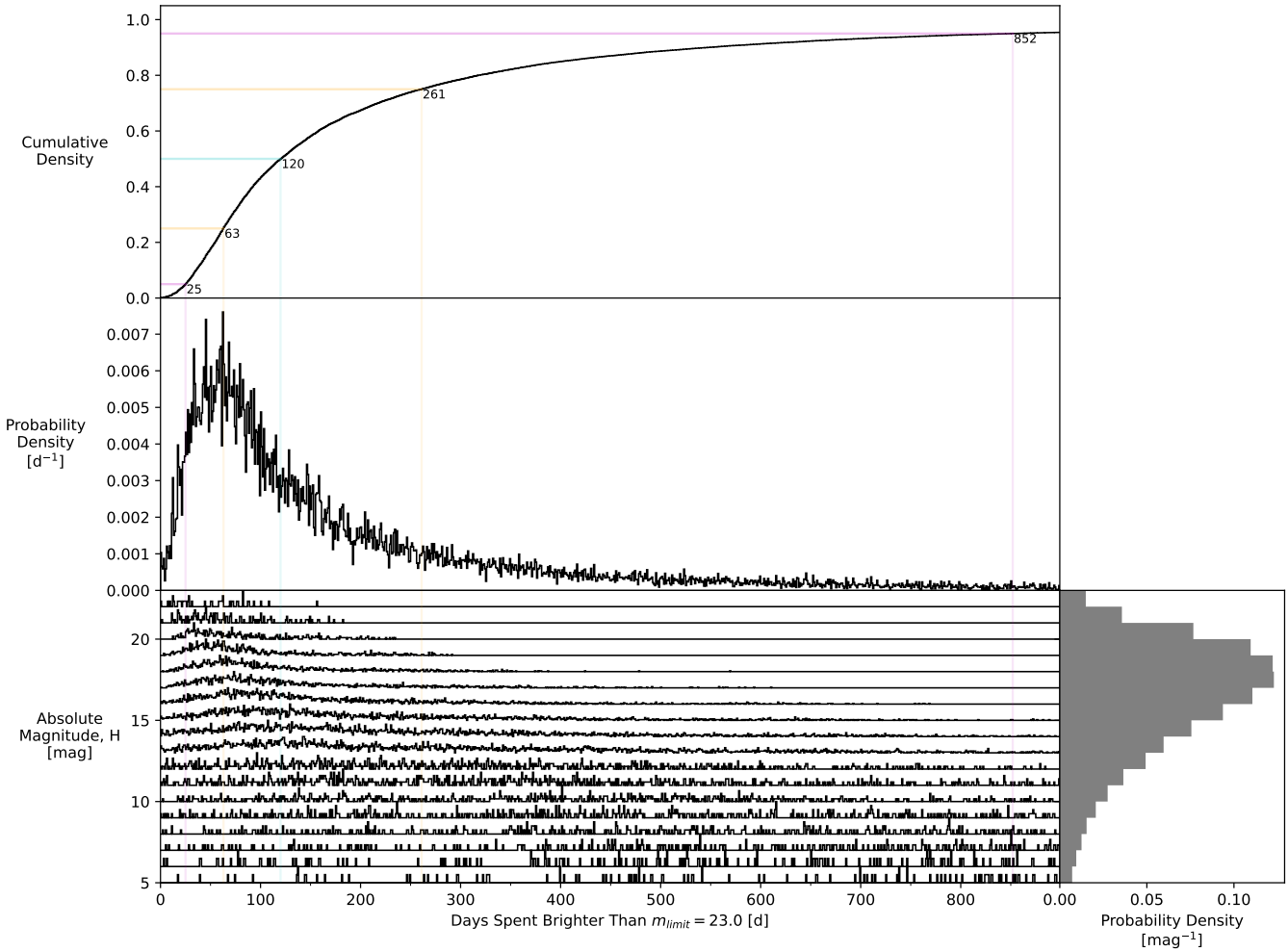

Figure 16. Cumulative and probability density functions for the amount of time an ISO will spend during its solar system passage above the magnitude limit for spectroscopic observation after its discovery in LSST if the object is discovered brighter than $m_r = 23$ (shown for $q_s = 2.8$). Different colored lines indicate percentiles of interest: 5th and 95th (magenta), 25th and 75th (orange), and 50th (cyan). Bottom left: qualitative probability density functions for each magnitude interval, normalized individually. This plot type we term a "tally plot." Bottom right: probability density function for the H_r distribution of discovered ISOs. Middle: probability density function for the whole population, produced by weighting each probability density function in the tally plot (bottom left) by the corresponding H_r probability density value (bottom right). Top: cumulative probability density function for the probability density function in the middle panel.

preperihelion (L. Inno et al. 2024). Compared to an inactive ISO of equal absolute magnitude, a cometary ISO will be more observable in a flux-limited survey. To the first order, cometary activity provides an equivalent improvement to an object's apparent magnitude as an increased absolute magnitude. Hence, for a qualitative estimate, the observability results for the absolute magnitude distribution slope $q_s = 2.5$ can be considered a potential proxy for a cometary ISO population. Compared to the steepest slope modeled $q_s = 4.0$, the absolute magnitude distribution with $q_s = 2.5$ produces a population of ISOs with lower absolute magnitudes (Figure 6), larger perihelia (Figure 8), an equal ratio of prograde and retrograde orbits (Figure 8), larger heliocentric distances at discovery (Figure 12), longer residence times, and a higher likelihood of discovery before perihelion (Figure 11). These results qualitatively agree with the comparisons between active and inactive ISOs from N. V. Cook et al. (2016) and T. Engelhardt et al. (2017).

7.6. Our New Understanding of ISOs in the Era of LSST

The Ōtautahi–Oxford population model predicts complex distributions of velocities, ages, and compositions for ISOs in the local neighborhood. By applying an absolute magnitude and other physical properties, we have inferred plausible orbital parameter distributions for the ISOs discovered in LSST.

The observed properties of LSST's ISO discoveries will be distinctly biased by the absolute magnitude distribution of the intrinsic Galactic population, including orbital parameters (perihelia, eccentricity, inclination, velocity at infinity), absolute magnitudes (median, and 3σ confidence interval), circumstances at discovery (heliocentric and geocentric distance, on-sky velocity, phase angle, time until perihelion), and observability in LSST (number of observations and tracklets, arc length, characterization window lengths). The subtlety here is that the *distributions* of these values for the LSST-discovered *population* will be evidence for the intrinsic absolute magnitude distribution, not their value for any single discovered object. The resulting debiased absolute magnitude distribution, representing the end sum of all Galactic ISO production processes, can then be used to infer the impact of different proposed processes.

Additionally, the number of ISOs discovered over the survey duration depends on the intrinsic absolute magnitude distribution; expectations vary by 2 orders of magnitude across a factor of $\sim$1.5 in the absolute magnitude slope q_s.

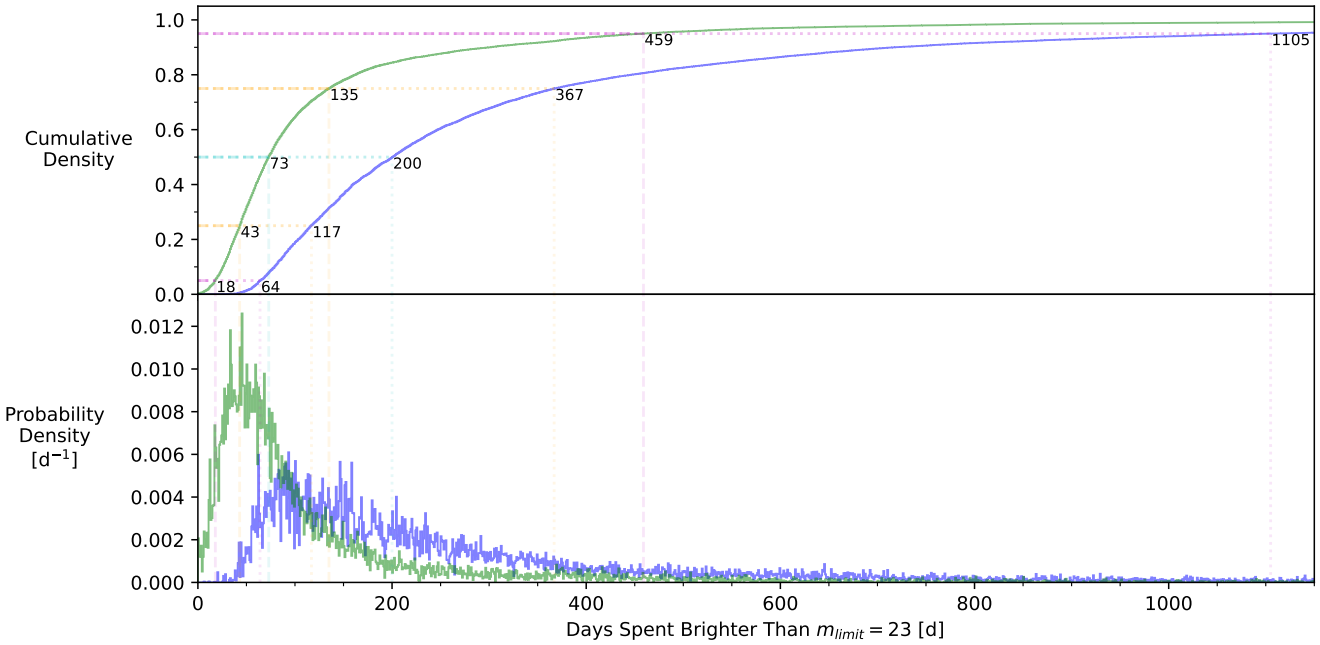

Figure 17. Similar to Figure 16, but comparing the amount of time ISOs discovered inbound (blue) or outbound (green) spend above the spectroscopic limit $m_r = 23$ after discovery.

However, the spatial number density of ISOs is linearly correlated to the number of discoveries. The result is a degeneracy, where a low absolute magnitude slope and a high number density will produce the same number of LSST discovered ISOs as a high absolute magnitude slope and a low number density. The distributions listed above must be correctly characterized in the LSST ISO sample to disentangle this degeneracy. This demonstrates how crucial it is to quantify observational biases to understand the population of ISOs that LSST will observe.

8. Conclusion

The LSST presents an unrivaled opportunity to discover a new sample of ISOs. We summarize our primary findings from a highly realistic simulation of its observations of the Ōtautahi–Oxford population model of ISOs:

1. ISOs are most likely to be found at the edge of observability, due to their single perihelion passage and observable sphere radius.
2. Small ISOs observed by LSST are harder to discover than large ISOs. The "limiting absolute magnitude" for ISOs in LSST is $H_r \approx 23$, and these objects are about 5 times less discoverable than the large observed ISOs with $H_r \leqslant 13$.
3. The absolute magnitude distribution slope of the intrinsic ISO population can be constrained within ± 0.5 with the discovery of $\sim$20−80 ISOs.
4. The discovery of a single ISO with $H_r \leqslant 10$ will strongly suggest a shallow slope for the intrinsic absolute magnitude distribution. In contrast, the discovery of an ISO similar to 1I/'Oumuamua ($H_r \sim 22.4$) or smaller would not provide any meaningful constraint.
5. The orbital parameter distributions of discovered ISOs—perihelia, eccentricity, inclination, and velocity at infinity—will be indicators of the intrinsic absolute magnitude distribution.
6. For absolute magnitude distribution slopes $2.5 \leqslant q_s \leqslant 4.0$ and spatial number density estimates from earlier surveys of $n \sim 10^{-1}$ au^{-3}, LSST will discover between 6 and 51 ISOs over its 10 yr.
7. ISOs in LSST will have biased orbit orientations (ω and Ω) and discovery time relative to perihelion due to being discovered by a southern sky survey. ISOs are equally likely to be discovered before as after perihelion.
8. The twilight microsurvey contributes <2% of LSST's ISO discoveries for all slopes q_s.
9. Most ISOs (>90%) will be immediately bright enough for spectroscopic follow-up at their discovery, and of these, most will stay above this brightness for about a month.
10. Regardless of individual absolute magnitude and the intrinsic absolute magnitude slope, 95% of ISOs will be bright enough for major ground-based and space telescope follow-up for $\geqslant$2 months. 1 in 20 ISOs will be observable for general follow-up for $\gtrsim$5 yr if the ISO luminosity function has $q_s = 2.8$.
11. The majority of ISOs discovered preperihelion will be found 60–360 days beforehand, potentially compatible with mission designs for storage-in-orbit with a suitable Δv budget.

Understanding the complex observability and discoverability of ISOs in LSST is vital for interpreting the LSST ISO sample, regardless of whether LSST contains any ISO detections. The probabilistic description of LSST's ISOs that we quantify offers a path to mitigate the negative impacts of "Hypothesizing After the Results are Known" (or "HARKing"), a scientific methodology that retrospectively encourages biases in the direction of future research. With only two members known so far, the field of small body Galactic studies is in an ideal position to prepare our models and theories of the little-known ISO population as we move toward the next generation of solar system surveys.

Acknowledgments

The authors would like to thank the reviewers for the constructive and thoughtful comments.

We thank the LSST Solar System Science Collaboration for manuscript feedback, particularly Sarah Greenstreet, Bryce Bolin, and Dusan Marceta, and the NEO Surveyor Science Workshop and Joe Masiero for helpful discussions and comments.

R.C.D. acknowledges previous support from the UC Doctoral Scholarship and Canterbury Scholarship administered by the University of Canterbury, a PhD research scholarship through M.T.B.'s Rutherford Discovery Fellowship grant, and LSSTC Enabling Science grant #2021-31 awarded by LSST Discovery Alliance. R.C.D. is currently funded by grant #361233 awarded by the Research Council of Finland to M. Granvik.

M.J.H. acknowledges support from the Science and Technology Facilities Council through grant ST/W507726/1.

M.T.B. and J.C.F. appreciate support by the Rutherford Discovery Fellowships from New Zealand Government funding, administered by the Royal Society Te Apārangi.

This work has made use of data from the European Space Agency (ESA) mission Gaia (https://www.cosmos.esa.int/gaia), processed by the Gaia Data Processing and Analysis Consortium (DPAC, https://www.cosmos.esa.int/web/gaia/dpac/consortium). Funding for the DPAC has been provided by national institutions, in particular the institutions participating in the Gaia Multilateral Agreement.

Software: astropy (Astropy Collaboration et al. 2013, 2018), numpy (C. R. Harris et al. 2020), pandas (The pandas development Team 2024), scipy (P. Virtanen et al. 2020).

Appendix A
Orbit Sampling

As detailed in Section 2 of this work, D. Marčeta (2023) sample the positions of ISOs at a given point in time. This is inefficient for simulating non-zero-length surveys, as it requires sampling a much bigger sphere than is actually observable, then propagating the objects along their orbits, many of which will never enter the observable sphere.

Instead, we sample the orbits directly, in terms of the preencounter velocity $\boldsymbol{v}_\infty$, impact parameter B, and angle of impact parameter φ. Note that the distribution of these orbits depends on the length of the survey: longer surveys sample more faster ISOs due to the refresh rate. This is due to the residence time $t_{\rm res}(\boldsymbol{v}_\infty, B, \varphi)$ of objects in the observable sphere becoming negligible compared to the survey length T; we demonstrate this below. These five parameters define the orbit; to get the sixth that defines the progress of an object along its orbit, we choose the time of perihelion τ, relative to the start of the LSST (e.g., 2025 May 1 for `baseline_v3.3_10yrs`). By symmetry, objects on an orbit are distributed uniformly in time; we therefore sample the perihelion time uniformly from $\tau \in [-\frac{t_{\rm res}}{2}, \frac{t_{\rm res}}{2} + T]$. This gives us a sample of ISOs and their orbits that will be in the observable sphere when the LSST is acquiring data.

The flux of ISOs onto an orbit ($\boldsymbol{v}_\infty$, B, φ) is given by D. Marčeta (2023), Equation (11):

$$F_{\boldsymbol{v}_\infty B\varphi} = nBv_\infty p_{\boldsymbol{v}_\infty}.$$

With the absolute value of the semimajor axis $A = GM_\odot/v_\infty^2 = -a$, perihelion $q = -A + \sqrt{A^2 + B^2}$, and maximum impact parameter for orbits entering the sphere at a given velocity $B_{\rm max} = \sqrt{r_{\rm h}^2 + 2Ar_{\rm h}}$, the residence time of object on an orbit (v_∞, B φ), the time it spends within the sphere of the radius $r_{\rm h}$ centered on the Sun, is

$$\begin{aligned} t_{\rm res}(\boldsymbol{v}_\infty, B) &= \frac{2}{v_\infty}\int_q^{r_{\rm h}} \frac{r_{\rm h} dr_{\rm h}}{\sqrt{r_{\rm h}^2 + 2Ar_{\rm h} - B^2}} \\ &= \frac{2}{v_\infty}\left(\sqrt{B_{\rm max}^2 - B^2} - A\log\left(\frac{\sqrt{B_{\rm max}^2 - B^2} + r_{\rm h} + A}{\sqrt{A^2 + B^2}}\right)\right). \end{aligned} \tag{A1}$$

Therefore the number of objects on an orbit ($\boldsymbol{v}_\infty$, B φ) that will spend any length of time within the observable sphere during the survey of the length T is equal to the sum of those in the sphere when the survey begins, plus the number that flow in over the time T:

$$\begin{aligned} \frac{dN}{d^3\boldsymbol{v}_\infty dBd\varphi} &= F_{\boldsymbol{v}_\infty B\varphi}(t_{\rm res}(\boldsymbol{v}_\infty, B, \varphi) + T) \\ &= 2nBp_{\boldsymbol{v}_\infty}(\sqrt{B_{\rm max}^2 - B^2} - A\log \\ &\quad \times \left(\frac{\sqrt{B_{\rm max}^2 - B^2} + r_{\rm h} + A}{\sqrt{A^2 + B^2}}\right) + \frac{v_\infty T}{2}\Bigg). \end{aligned} \tag{A2}$$

For $T = 0$, this equals the distribution of orbits of ISOs within a sphere of the radius $r_{\rm h}$ at a single moment in time, i.e., the distribution of D. Marčeta (2023). For $T \gg t_{\rm res}$, the ISOs already in the sphere when the survey begins is negligible compared to those that have flowed in since, so the distribution is dominated by the refreshing population—this is the volume-sampling weighted distribution used in M. J. Hopkins et al. (2025) ($q < r_{\rm h}$ in Table 1). φ is drawn uniformly from 0 to 2π independently of all other parameters, so we marginalize over this, and writing $x = B/B_{\rm max}$, $A' = A/B_{\rm max}$ and noting $r_{\rm h} + A = \sqrt{A^2 + B_{\rm max}^2} = B_{\rm max}\sqrt{A'^2 + 1}$ give

$$\begin{aligned} \frac{dN}{d^3\boldsymbol{v}_\infty dB} &= 4\pi nB_{\rm max}^2 p_{\boldsymbol{v}_\infty}(x\sqrt{1 - x^2} - A'x \\ &\quad \times \log\left(\frac{\sqrt{1 - x^2} + \sqrt{A'^2 + 1}}{\sqrt{A'^2 + x^2}}\right) + \frac{v_\infty T}{2B_{\rm max}}x\Bigg). \end{aligned} \tag{A3}$$

To sample $\boldsymbol{v}_\infty$ and B, we need the cumulative distribution function of B at given values of $\boldsymbol{v}_\infty$. First, we integrate up to a given B:

$$\begin{aligned} \int_0^B \frac{dN}{d^3\boldsymbol{v}_\infty dB} dB &= 4\pi nB_{\rm max}^3 p_{\boldsymbol{v}_\infty}\int_0^x (x\sqrt{1 - x^2} - A'\, x\log \\ &\quad \times \left(\frac{\sqrt{1 - x^2} + \sqrt{A'^2 + 1}}{\sqrt{A'^2 + x^2}}\right) + \frac{v_\infty T}{2B_{\rm max}}x\Bigg)dx \\ &= 4\pi nB_{\rm max}^3 p_{\boldsymbol{v}_\infty}\Bigg(\frac{1 - (1 - x^2)^{3/2}}{3} - \frac{A'}{2} \\ &\quad \times \left((A'^2 + x^2)\log\left(\frac{\sqrt{1 - x^2} + \sqrt{A'^2 + 1}}{\sqrt{A'^2 + x^2}}\right)\right. \\ &\quad - A'^2\log\left(\frac{1 + \sqrt{A'^2 + 1}}{A'}\right) - \sqrt{A'^2 + 1}\sqrt{1 - x} \\ &\quad \left. + \sqrt{A'^2 + 1}\right) + \frac{v_\infty T x^2}{4B_{\rm max}}\Bigg). \end{aligned} \tag{A4}$$

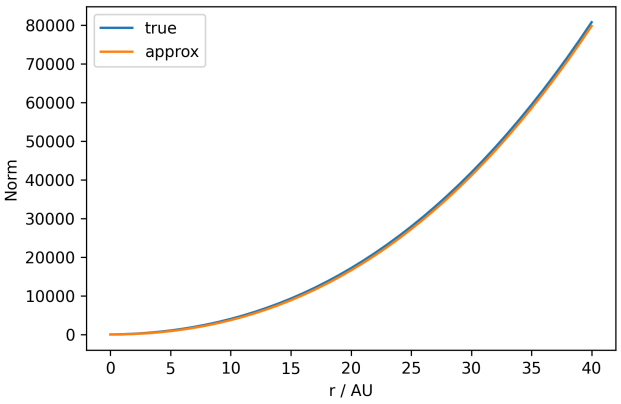

Figure 18. A comparison of the normalization of the distribution in Equation (A5) to its approximation in Equation (A6) for different observable spheres of radius r, showing it to be a good approximation.

When integrated to $B = B_{\max}$, or $x = 1$, this integral is equal to the velocity distribution of orbits passing through the sphere

$$\frac{dN}{d^3\boldsymbol{v}_\infty} = 4\pi n B_{\max}^3 \left(\frac{1}{3} - \frac{A'}{2}\left(\sqrt{A'^2+1} - A'^2 \log\left(\frac{1+\sqrt{A'^2+1}}{A'}\right)\right) + \frac{v_\infty T}{4B_{\max}}\right) \cdot p_{\boldsymbol{v}_\infty}. \quad \text{(A5)}$$

Equation (A4) divided by Equation (A5) is equal to the cumulative distribution function of B given a value of $\boldsymbol{v}_\infty$: $\mathrm{CDF}(B|\boldsymbol{v}_\infty)$.

We can now start sampling! Equation (A5) gives the distribution of preencounter velocities of the ISOs passing through the sphere. Since the "underlying ISO distribution" (Table 1 of M. J. Hopkins et al. 2025) corresponds to $p_{\boldsymbol{v}_\infty}$, we reweight those samples by the factor in front of $p_{\boldsymbol{v}_\infty}$ in Equation (A5) and resample them to get a sample of $\boldsymbol{v}_\infty$. For each $\boldsymbol{v}_\infty$ in this sample, we can evaluate the cumulative distribution $\mathrm{CDF}(B|\boldsymbol{v}_\infty)$, invert it, and draw a value of B. Penultimately, for each of these ($\boldsymbol{v}_\infty$, B) pairs, we draw a perihelion time τ from $\mathrm{Uniform}(-t_{\mathrm{res}}/2, t_{\mathrm{res}}/2 + T)$ where t_{res} is given by Equation (A1). And finally, for each ($\boldsymbol{v}_\infty$, B, τ), we draw a value of φ from $\mathrm{Uniform}(0, 2\pi)$.

The integral of Equation (A5) over $\boldsymbol{v}_\infty$ is equal to the number of objects entering the observable sphere of the radius r_{h} over the survey length T. Since this is difficult to calculate for the nonanalytic Ōtautahi–Oxford model velocity distribution $p_{\boldsymbol{v}_\infty}$, we approximate this with

$$\int \frac{dN}{d^3\boldsymbol{v}_\infty} d^3\boldsymbol{v}_\infty \approx n \cdot \left(\frac{4}{3}\pi r_{\mathrm{h}}^3 + \pi r_{\mathrm{h}}^2 T(0.029\ \mathrm{au\ day^{-1}})\right). \quad \text{(A6)}$$

A comparison of this approximation to the true value of the integral is plotted in Figure 18, showing it to be very accurate.

Appendix B
The Absolute Magnitude Shallow Slope Effect

ISOs simulated from an absolute magnitude distribution with $q_s = 2.0$ ($\alpha = 0.2$) produce an unusual probability density function for the discovered objects in the sample (Figure 19): more objects with low H (large diameter) are discovered than objects with high H (small diameter), despite being less common. This is due to the ISO population being unbounded in space. Larger objects have a larger observable sphere, so at some critical slope q, the decreasing frequency of larger objects is counteracted by the increase in the number of objects within the observable sphere. For size distributions with slopes less than this critical value, the number of objects of a given size contained within the corresponding observable sphere increases with size.

This effect is unique to the simulation of ISOs. Unlike any other solar system small body population, ISOs do not occupy a localized region of the solar system. For all small body populations bound to the solar system, there will always be some heliocentric distance at which the population is complete. However, ISOs are a Galactic population, so spatial population completeness only occurs across the entire Galaxy.

To constrain the critical slope value, we numerically modeled two additional slope values, $q_s = 2.125$ and $q_s = 2.25$. The total weights (Equation (4)) for each slope q value appear approximately parabolic in H_r (Figure 19). For $q_s \geqslant 2.5$, the minimum weighting always occurs for $5 \leqslant H_r \leqslant 6$. As the slope q_s decreases, the minimum weighting shifts to larger values of H_r (smaller objects). The transition occurs around $q_{s,\mathrm{crit}} \approx 2.25{-}2.5$, or $\alpha_{\mathrm{crit}} \approx 0.25{-}0.3$.

This can also be determined analytically. For large objects (small H_r), as per Equation (3), objects of the absolute magnitude H_r are visible out to a distance of approximately $r \approx 10^{(m_{\mathrm{lim}}-H_r)/10}$ au. For these objects, the refreshing population is negligible, so the observable volume is well approximated by a sphere with a volume $\propto r^3$. For a power-law absolute magnitude distribution $dN/dH \propto 10^{\alpha H_r}$, the number of visible objects of magnitude H is proportional to $r^3 10^{\alpha H_r} = 10^{3m_{\mathrm{lim}}/10} \cdot 10^{(\alpha-3/10)H_r}$. Thus, there is a critical value $\alpha_{\mathrm{crit}} = 0.3$, or $q_{s,\mathrm{crit}} = 2.5$. Below this value, the number of visible objects increases indefinitely as H decreases.

Both analyses indicate that single-slope absolute magnitude distributions with $q_s < 2.5$ represent an improbable model for ISOs. This is because these absolute magnitude distributions would produce a distribution of detected ISOs that increases indefinitely with decreasing H_r; thus, we would expect to discover more large ISOs than small ISOs. Instead, 1I/'Oumuamua, the one known asteroidal ISO, had an absolute magnitude of $H_r \sim 22.4$, placing it among the smallest ISOs we expect to discover. Hence, we consider $q_s = 2.5$ the most physically reasonable lower limit for the absolute magnitude distribution slope and use it accordingly for the rest of this work.

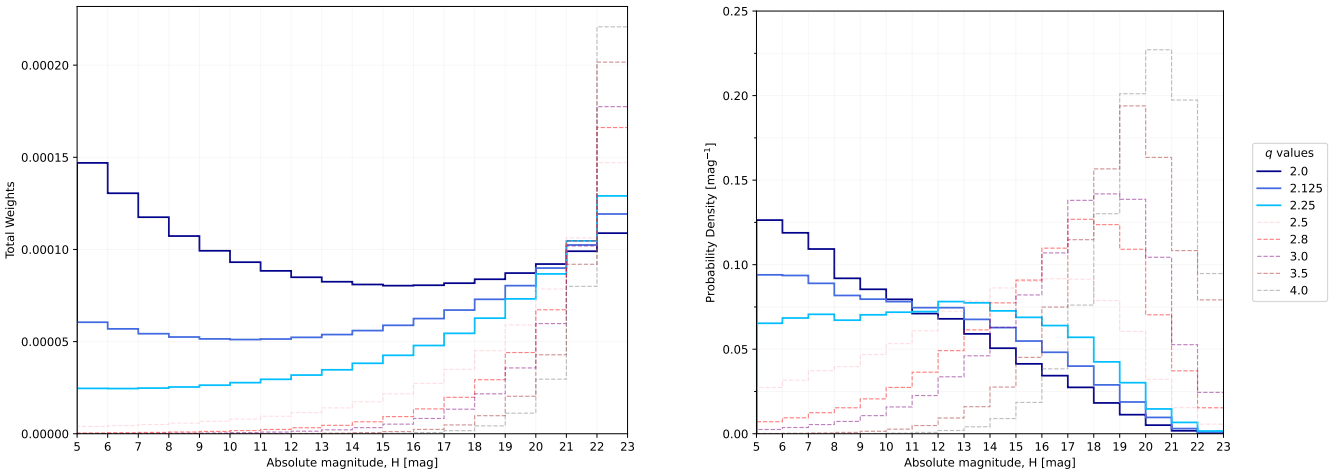

Figure 19. A series of numerical simulations with different absolute magnitude distribution slopes in the range $q_s = [2.0, 4.0]$. Left: combined orbital and H_r-distribution weightings given by Equation (4). Right: probability density functions for the discovered ISO population for each slope q_s.

Appendix C
Expected Numbers of ISOs

Here, we compute the number of ISOs that will be discovered in LSST, using the observational and discovery efficiencies of ISOs in LSST determined for different absolute magnitude distributions.

First, we calculate the total observable volume LSST will survey during its 10 yr operation. For an object of the absolute magnitude $H_r = 5$ and assumed 5σ limiting r-band magnitude $m_5 = 25$, the corresponding observable sphere has a radius given by Equation (3):

$$r_{H_{\rm min}}(H_{\rm min} = 5) = \frac{1}{2}\left(1 + \sqrt{1 + 4 \times 10^{\frac{25-5}{5}}}\right) \text{au} = 100.5 \text{ au}. \quad \text{(C1)}$$

The volume of space surveyed by LSST over its duration $T = 3652.42$ days is therefore

$$V = \frac{4}{3}\pi(100.5)^3 + \pi(100.5)^2(3652.42 \times 0.029) = 7.61 \times 10^6 \text{ au}^3 \quad \text{(C2)}$$

where 0.029 is the average velocity of ISOs relative to the Sun in astronomical units per day. The number of ISOs in this volume with the absolute magnitude H_r is

$$N_{\rm sph} = nV = n(7.61 \times 10^6) \quad \text{(C3)}$$

where n is the number density for objects with H_r in per cubic astronomical units.

The number of ISOs in the ΔH interval $H_r = [H_{\rm min}, H_{\rm max}]$, where $H_{\rm max} = H_{\rm min} + 1$ of a single-slope power-law absolute magnitude distribution, is given by

$$N_{\Delta H} \propto 10^{\alpha H_{\rm max}} - 10^{\alpha H_{\rm min}} \quad \text{(C4)}$$

where α is defined in relation to the slope parameter q_s by $q_s = 5\alpha + 1$. The number of ISOs across all H_r intervals is normalized such that $N_{H=22}$ is equal to $N_{\rm sph}$ for a number density defined with respect to objects with the absolute magnitude $H_r = 22$:

$$N_{\Delta H} = [10^{\alpha H_{\rm max}} - 10^{\alpha H_{\rm min}}]\frac{N_{\rm sph}}{10^{22\alpha}} = n(7.61 \times 10^6)\left[\frac{10^{\alpha H_{\rm max}} - 10^{\alpha H_{\rm min}}}{10^{22\alpha}}\right]. \quad \text{(C5)}$$

The total number of ISOs in the range $H_r = [5, 23]$ considered in this work that enter the ~100 au radius sphere during LSST is therefore

$$N_{\Delta H} = n(7.61 \times 10^6)\left[\frac{10^{23\alpha} - 10^{5\alpha}}{10^{22\alpha}}\right] = \begin{cases} 1.52 \times 10^7, & q_s = 2.5 \\ 3.03 \times 10^7, & q_s = 4.0 \end{cases} \quad \text{(C6)}$$

for typical modern estimates $n \sim 0.1$ au^{-3} (K. J. Meech et al. 2017; A. Do et al. 2018).

Next, the orbital sampling weightings for each ΔH interval are calculated by dividing the observable sphere volume at the given $H_{\rm min}$ value by the largest observable sphere volume:

$$w = \frac{\frac{4}{3}\pi r_{H_{\rm min}}^3 + \pi r_{H_{\rm min}}^2(0.029T)}{\frac{4}{3}\pi 100.5^3 + \pi 100.5^2(0.029T)} = \frac{\frac{4}{3}\pi r_{H_{\rm min}}^3 + 105.9\pi r_{H_{\rm min}}^2}{7.61 \times 10^6}. \quad \text{(C7)}$$

This gives the fraction of objects that enter the ISO population's observable sphere and reach their H_r-dependent observable sphere to be potentially observed in LSST. For example, the interval $H_r = [22, 23]$ where $r_{H_{\rm min}} = r_{H_{\rm min}}(H_{\rm min} = 22)$ has the weighting $w = 2.95 \times 10^{-4}$. This means that if there are $(2.95 \times 10^{-4})^{-1} \approx 3400$ ISOs in the population observable sphere, only one object reaches the H_r-dependent observable sphere. Therefore, the number of ISOs of the absolute magnitude H_r that reach their

H_r-dependent observable sphere is

$$N_{\text{observable},\Delta H} = N_{\Delta H} \times w = n\left[\frac{10^{\alpha(H_{\max})} - 10^{\alpha H_{\min}}}{10^{22\alpha}}\right] \times \left(\frac{4}{3}\pi r_{H_{\min}}^3 + 105.9\pi r_{H_{\min}}^2\right). \quad \text{(C8)}$$

This is then multiplied by the fraction of ISOs $f_{\Delta H}$ in the relevant simulation, which is discovered in our LSST survey simulation to get the number of ISOs in the ΔH interval that are discovered during LSST:

$$N_{\text{discovered},\Delta H} = N_{\text{observable},\Delta H} \times f_{\Delta H} = f_{\Delta H} \times n\left[\frac{10^{\alpha H_{\max}} - 10^{\alpha H_{\min}}}{10^{22\alpha}}\right] \times \left(\frac{4}{3}\pi r_{H_{\min}}^3 + 105.9\pi r_{H_{\min}}^2\right). \quad \text{(C9)}$$

The discoveries across all H_r intervals are summed to give the total discovered ISOs:

$$N_{\text{discovered,total}} = \sum_{H_{\min}=5}^{22} N_{\text{discovered},\Delta H} = n\sum_{H_{\min}=5}^{22} f_{\Delta H}\left[\frac{10^{\alpha H_{\max}} - 10^{\alpha H_{\min}}}{10^{22\alpha}}\right] \times \left(\frac{4}{3}\pi r_{H_{\min}}^3 + 105.9\pi r_{H_{\min}}^2\right). \quad \text{(C10)}$$

We obtain the following prediction for our absolute magnitude distributions:

$$N_{\text{discovered,total}} = \begin{cases} 514n, & q_s = 2.5 \\ 244n, & q_s = 2.8 \\ 168n, & q_s = 3.0 \\ 87.1n, & q_s = 3.5 \\ 58.6n, & q_s = 4.0. \end{cases} \quad \text{(C11)}$$

For number density values of $n = 0.1\,\text{au}^{-3}$ (A. Do et al. 2018) and $n = 0.24\,\text{au}^{-3}$ (K. J. Meech et al. 2017) for $H_r \leqslant 22$ (both determined after the discovery of 1I/'Oumuamua), our prediction is 6–51 and 14–123 ISOs, respectively. Therefore, we can expect LSST to discover $\sim 10^0$–10^2 ISOs during its 10 yr nominal survey.

ORCID iDs

Rosemary C. Dorsey https://orcid.org/0000-0002-8910-1021
Matthew J. Hopkins https://orcid.org/0000-0001-6314-873X
Michele T. Bannister https://orcid.org/0000-0003-3257-4490
Samantha M. Lawler https://orcid.org/0000-0001-5368-386X
Chris Lintott https://orcid.org/0000-0001-5578-359X
Alex H. Parker https://orcid.org/0000-0002-6722-0994
John C. Forbes https://orcid.org/0000-0002-1975-4449

References

A'Hearn, M. F., Belton, M. J. S., Delamere, W. A., et al. 2005, Sci, 310, 258
Alvarez-Candal, A. 2024, A&A, 685, A29
Alvarez-Candal, A., & Licandro, J. 2006, A&A, 458, 1007
Anderson, T. W., & Darling, D. A. 1952, Ann. Math. Stat., 23, 193
Andreoni, I., Margutti, R., Banovetz, J., et al. 2024, arXiv:2411.04793
Astropy Collaboration, Price-Whelan, A. M., Sipőcz, B. M., et al. 2018, AJ, 156, 123
Astropy Collaboration, Robitaille, T. P., Tollerud, E. J., et al. 2013, A&A, 558, A33
Bannister, M. T., Opitom, C., Fitzsimmons, A., et al. 2020, arXiv:2001.11605
Bannister, M. T., Schwamb, M. E., Fraser, W. C., et al. 2017, ApJL, 851, L38
Bernstein, G., & Khushalani, B. 2000, AJ, 120, 3323
Bianco, F. B., Ivezić, Ž., Jones, R. L., et al. 2022, ApJS, 258, 1
Bianco, F. B., Jones, L., Ivezić, Ž., Ritz, S. & the Rubin Project Science Team 2022, Updated Estimates of the Rubin System Throughput and Expected LSST Image Depth, Tech. Rep. PSTN-054, NSF-DOE Vera C. Rubin Observatory
Boe, B., Jedicke, R., Meech, K. J., et al. 2019, Icar, 333, 252
Bolin, B. T., Ahumada, T., van Dokkum, P., et al. 2022, MNRAS, 517, L49
Bolin, B. T., Masci, F. J., Ye, Q. Z., et al. 2020, 2020 AV2 2020-A99, Minor Planet Center https://www.minorplanetcenter.net/mpec/K20/K20A99.html
Bottke, W. F., Durda, D. D., Nesvorný, D., et al. 2005, Icar, 175, 111
Bottke, W. F., Vokrouhlický, D., Marschall, R., et al. 2023, PSJ, 4, 168
Bowell, E., Hapke, B., Domingue, D., et al. 1989, Application of Photometric Models to Asteroids, in Asteroids II, ed. R. P. Binzel, T. Gehrels, & M. S. Matthews (Tuscon, AZ: Univ. Arizona Press), 524
Brasser, R., Duncan, M. J., & Levison, H. F. 2006, Icar, 184, 59
Claver, C. F. & LSST Systems Engineering Integrated Project Team 2024, LSST Observatory System Specifications (OSS), Tech. Rep., LSST Corporation LSE-030, NSF-DOE Vera C. Rubin Observatory https://docushare.lsst.org/docushare/dsweb/Get/LSE-030
Colazo, M., Duffard, R., & Weidmann, W. 2021, MNRAS, 504, 761
Cook, N. V., Ragozzine, D., Granvik, M., & Stephens, D. C. 2016, ApJ, 825, 51
de León, J., Licandro, J., de la Fuente Marcos, C., et al. 2020, MNRAS, 495, 2053
Denneau, L., Jedicke, R., Grav, T., et al. 2013, PASP, 125, 357
Do, A., Tucker, M. A., & Tonry, J. 2018, ApJL, 855, L10
Dobson, M. M., Schwamb, M. E., Benecchi, S. D., et al. 2023, PSJ, 4, 75
Dotto, E., Barucci, M. A., & de Bergh, C. 2003, CRPhy, 4, 775
Eggl, S., Jones, L., & Juric, M. 2019, LSST Asteroid Discovery Rates, Tech. Rep. DMTN-109, NSF-DOE Vera C. Rubin Observatory https://dmtn-109.lsst.io/
Engelhardt, T., Jedicke, R., Vereš, P., et al. 2017, AJ, 153, 133
Farnocchia, D., Cioci, D. B., & Milani, A. 2013, CeMDA, 116, 21
Fernandez, J. A. 1978, Icar, 34, 173
Fitzsimmons, A., Meech, K., Matrà, L., & Pfalzner, S. 2024, Interstellar Objects and Exocomets, in Comets III, ed. K. Meech (Tuscon, AZ: Univ. Arizona Press)
Flekkøy, E. G., & Toussaint, R. 2023, MNRAS, 523, L9
Forbes, J. C., Bannister, M. T., Lintott, C., et al. 2025, ApJ, 988, 121
Forbes, J. C., & Loeb, A. 2019, ApJL, 875, L23
Francis, P. J. 2005, ApJ, 635, 1348
Fraser, W. C. 2025, Detecting Moving Objects with Machine Learning, in Machine Learning for Small Bodies in the Solar System, ed. V. Carruba, E. Smirnov, & D. Oszkiewicz (Amsterdam: Elsevier)
Fraser, W. C., Porter, S. B., Peltier, L., et al. 2024, PSJ, 5, 227
Fraser, W. C., Pravec, P., Fitzsimmons, A., et al. 2018, NatAs, 2, 383
Gaia Collaboration, Prusti, T., de Bruijne, J. H. J., et al. 2016, A&A, 595, A1
Gaia Collaboration, Vallenari, A., Brown, A. G. A., et al. 2023, A&A, 674, A1
Gundlach, B., Blum, J., Skorov, Y. V., & Keller, H. U. 2012, arXiv:1203.1808
Harris, C. R., Millman, K. J., van der Walt, S. J., et al. 2020, Natur, 585, 357
Holman, M. J., Payne, M. J., Blankley, P., Janssen, R., & Kuindersma, S. 2018, AJ, 156, 135
Hoover, D. J., Seligman, D. Z., & Payne, M. J. 2022, PSJ, 3, 71
Hopkins, M. J., Bannister, M. T., & Lintott, C. 2025, AJ, 169, 78
Hopkins, M. J., Lintott, C., Bannister, M. T., Mackereth, J. T., & Forbes, J. C. 2023, AJ, 166, 241
Hu, J. A., Rawls, M. L., Yoachim, P., & Ivezić, Ž. 2022, ApJL, 941, L15
Hui, M.-T., Ye, Q.-Z., Föhring, D., Hung, D., & Tholen, D. J. 2020, AJ, 160, 92
Inno, L., Scuderi, M., Bertini, I., et al. 2025, Icar, 429, 116443
Jackson, S. L., Rozitis, B., Dover, L. R., et al. 2022, MNRAS, 513, 3076
Jewitt, D. 2015, AJ, 150, 201
Jewitt, D., & Hsieh, H. H. 2024, The Asteroid-comet Continuum, in Comets III, ed. K. Meech (Tuscon, AZ: Univ. Arizona Press)
Jewitt, D., Hui, M.-T., Kim, Y., et al. 2020, ApJL, 888, L23
Jewitt, D., & Luu, J. 2019, ApJL, 886, L29
Jewitt, D., Luu, J., Rajagopal, J., et al. 2017, ApJL, 850, L36
Jewitt, D., & Seligman, D. Z. 2023, ARA&A, 61, 197

Jones, G. H., Snodgrass, C., Tubiana, C., et al. 2024, SSRv, 220, 9
Jones, R. L., Slater, C. T., Moeyens, J., et al. 2018, Icar, 303, 181
Juric, M., Eggl, S., Moeyens, J., & Jones, L. 2020, Proposed Modifications to Solar System Processing and Data Products DMTN-087, NSF-DOE Vera C. Rubin Observatory https://dmtn-087.lsst.io/
Kiselev, N. N., & Chernova, G. P. 1981, Icar, 48, 473
Królikowska, M., & Dybczyński, P. A. 2019, MNRAS, 484, 3463
Lambrechts, M., & Morbidelli, A. 2016, AAS/DPS Meeting, 48, 105.08
Landau, D., Donitz, B., & Karimi, R. 2023, AcAau, 206, 133
Levine, W. G., & Jedicke, R. 2023, Icar, 396, 115501
Levine, W. G., Taylor, A. G., Seligman, D. Z., et al. 2023, PSJ, 4, 124
Levison, H. F., & Duncan, M. J. 1997, Icar, 127, 13
Licandro, J., Alí-Lagoa, V., Tancredi, G., & Fernández, Y. 2016, A&A, 585, A9
Lineweaver, C. H., & Norman, M. 2010, The Potato Radius: A Lower Minimum Size for Dwarf Planets, in 9th Australian Space Science Conf., ed. W. Short & I. Cairns (Sydney: National Space Society of Australia Ltd) https://eprints.qut.edu.au/32917/1/9ASSC_proceedings_M_Zbik.pdf
Lintott, C., Bannister, M. T., & Mackereth, J. T. 2022, ApJL, 924, L1
LSST Science Collaboration, Abell, P. A., Allison, J., et al. 2009, arXiv:0912.0201
LSST Survey Cadence Optimization Committee 2024, Survey Cadence Optimization Committee's Phase 3 Recommendations, Tech. Rep. PSTN-056, NSF-DOE Vera C. Rubin Observatory https://pstn-056.lsst.io/
Lu, X.-P., & Jewitt, D. 2019, AJ, 158, 220
Mainzer, A. K., Masiero, J. R., Abell, P. A., et al. 2023, PSJ, 4, 224
Marčeta, D. 2023, A&C, 42, 100690
Marčeta, D., & Novaković, B. 2020, MNRAS, 498, 5386
Marčeta, D., & Seligman, D. Z. 2023, PSJ, 4, 230
Marinelli, M., & Dressel, L. 2024, WFC3 Instrument Handbook for Cycle 32 v. 16.0 (Baltimore, MD: STScI)
Mashchenko, S. 2019, MNRAS, 489, 3003
Masiero, J. R., Mainzer, A. K., Bauer, J. M., et al. 2021, PSJ, 2, 162
Matthews, B. C., Krivov, A. V., Wyatt, M. C., Bryden, G., & Eiroa, C. 2014, in Protostars and Planets VI, ed. H. Beuther et al. (Tuscon, AZ: Univ. Arizona Press), 521
McGlynn, T. A., & Chapman, R. D. 1989, ApJL, 346, L105
McNeill, A., Hora, J. L., Gustafsson, A., Trilling, D. E., & Mommert, M. 2019, AJ, 157, 164
Meech, K. J., Weryk, R., Micheli, M., et al. 2017, Natur, 552, 378
Micheli, M., Farnocchia, D., Meech, K. J., et al. 2018, Natur, 559, 223
IAU Minor Planet Center 2019, MPEC 2019-R106: COMET C/2019 Q4 (Borisov) 2019-R106, IAU Minor Planet Center https://www.minorplanetcenter.net/mpec/K19/K19RA6.html
Moeyens, J., Jurić, M., Ford, J., et al. 2021, AJ, 162, 143
Mommert, M., McNeill, A., Trilling, D. E., Moskovitz, N., & Delbo', M. 2018, AJ, 156, 139
Moro-Martín, A. 2018, ApJ, 866, 131
Moro-Martín, A., Turner, E. L., & Loeb, A. 2009, ApJ, 704, 733
Myers, J., Jones, L., & Axelrod, T. 2013, LSST Moving Object Pipeline System Design LDM-156, NSF-DOE Vera C. Rubin Observatory https://docushare.lsst.org/docushare/dsweb/Services/LDM-156
Naghib, E., Yoachim, P., Vanderbei, R. J., Connolly, A. J., & Jones, R. L. 2019, AJ, 157, 151
O'Mullane, W., Allbery, R., AlSayyad, Y., et al. 2024, Rubin Observatory Data Security Standards Implementation DMTN-199, NSF-DOE Vera C. Rubin Observatory https://dmtn-199.lsst.io/
Opitom, C., Fitzsimmons, A., Jehin, E., et al. 2019, A&A, 631, L8
'Oumuamua ISSI Team, Bannister, M. T., Bhandare, A., et al. 2019, NatAs, 3, 594
Petit, J.-M., Gladman, B., Kavelaars, J. J., et al. 2023, ApJL, 947, L4
Pfalzner, S., Aizpuru Vargas, L. L., Bhandare, A., & Veras, D. 2021, A&A, 651, A38
Pfalzner, S., & Bannister, M. T. 2019, ApJL, 874, L34
Portegies Zwart, S. 2021, A&A, 647, A136
Raymond, S. N., Kaib, N. A., Armitage, P. J., & Fortney, J. J. 2020, ApJL, 904, L4
Rice, M., & Laughlin, G. 2019, ApJL, 884, L22
Ridpath, I. 2012, in A Dictionary of Astronomy, ed. I. Ridpath (2nd ed.; Oxford: Oxford Univ. Press)
Rivkin, A. S., & Cheng, A. F. 2023, NatCo, 14, 1003
Robinson, J. E., Fitzsimmons, A., Young, D. R., et al. 2024a, MNRAS, 531, 304
Robinson, J. E., Schwamb, M. E., Jones, R. L., et al. 2025, ApJS, 279, 9
Sánchez, J. P., Morante, D., Hermosin, P., et al. 2021, AcAau, 188, 265
Schönrich, R., Binney, J., & Dehnen, W. 2010, MNRAS, 403, 1829
Schwamb, M. E., Jones, R. L., Yoachim, P., et al. 2023, ApJS, 266, 22
Seligman, D., & Laughlin, G. 2018, AJ, 155, 217
Sen, A. K., & Rana, N. C. 1993, A&A, 275, 298
Shevchenko, V. G., Belskaya, I. N., Slyusarev, I. G., et al. 2012, Icar, 217, 202
Simon, J. B., Armitage, P. J., Li, R., & Youdin, A. N. 2016, ApJ, 822, 55
Snodgrass, C., Tubiana, C., Fitzsimmons, A., & Lowry, S. C. 2011, in EPSC-DPS Joint Meeting 2011, 1524
Stern, S. A. 1990, PASP, 102, 793
Stern, S. A., Protopapa, S., Freeman, M., et al. 2024, P&SS, 241, 105850
The pandas development Team 2024, pandas-dev/pandas: Pandas, v2.2.3, Zenodo, doi:10.5281/zenodo.3509134
Thirouin, A., Moskovitz, N. A., Binzel, R. P., et al. 2018, ApJS, 239, 4
Trilling, D. E., Robinson, T., Roegge, A., et al. 2017, ApJL, 850, L38
Tyson, J. A., Ivezić, Ž., Bradshaw, A., et al. 2020, AJ, 160, 226
Virtanen, P., Gommers, R., Oliphant, T. E., et al. 2020, NatMe, 17, 261
Whipple, F. L. 1975, AJ, 80, 525
Willmer, C. N. A. 2018, ApJS, 236, 47
Yoachim, P., & Becker, M. R. 2023, lsst-sims/sims_featureScheduler_runs3.3: DOI (v1.0.1), Zenodo, doi:10.5281/zenodo.10126869